Journal of Magnetic Resonance **150,** 81–99 (2001)
doi:10.1006/jmre.2001.2310, available online at http://www.idealibrary.com on IDEAL®

Adiabatic Dipolar Recoupling in Solid-State NMR: The DREAM Scheme

René Verel, Matthias Ernst, and Beat H. Meier [1]

Laboratory of Physical Chemistry, ETH Honggerberg, CH-8093 Zurich, Switzerland

Received November 27, 2000; revised February 16, 2001

A theoretical treatment of the DREAM adiabatic homonuclear recoupling experiment is given using Floquet theory. An effective Hamiltonian is derived analytically and the time evolution of the density operator in the adiabatic limit is described. Shape cycles are proposed and characterized experimentally. Application to spin-pair filtering and as a mixing period in a 2D correlation experiment is explored and the experimental results are compared to theoretical predictions and exact numerical simulations.

1. INTRODUCTION

Most NMR structure-determination schemes are based on dipolar interactions which depend in a simple and direct way on internuclear distances and bond angles. In anisotropic phase (e.g., in static solids or oriented liquids), the system Hamiltonian explicitly contains dipolar terms which are manifest in the spectrum as line splittings or as a polarization-transfer mechanism during the mixing time in a two-dimensional correlation experiment. In "straightforward" magic-angle spinning (MAS) spectroscopy, however, the dipolar interaction is absent in the averaged time-independent ("secular") system Hamiltonian. Time-dependent ("nonsecular") dipolar terms are still present but usually have, for spinning frequencies greatly exceeding the magnitude of these interactions, a negligible influence on the time evolution of the spin system.

In recent years, a number of homonuclear and heteronuclear recoupling schemes have been developed which reintroduce secular dipolar contributions into the system Hamiltonian under MAS. The recoupling is often achieved by applying RF pulses or a continuous-wave (cw) RF field during the recoupling period. In this publication, we concentrate on the homonuclear case (*1–17*).

In multiply ^{13}C-labeled compounds, the spectral resolution often increases with increasing spinning frequency and it is, therefore, beneficial to develop recoupling schemes that can be applied at high MAS frequencies. For many pulsed recoupling schemes, the ratio of RF-field strength (in frequency units) to spinning frequency is between 3 and 10. This makes it difficult to successfully apply most of the existing recoupling schemes at spinning frequencies above 25 kHz. A noticeable exception from this RF-field strength requirement is the HORROR experiment (*9*) which uses RF fields which are by a factor of 2 lower than the MAS frequency. Due to the low RF-field strength, the HORROR experiment shows a very strong sensitivity to RF-field inhomogeneity and chemical-shift offsets.

Recently, we have demonstrated that an adiabatic passage through the HORROR recoupling condition, obtained by an RF-amplitude modulation, is able to remove the above-mentioned drawbacks of the HORROR experiment while retaining the favorable RF-amplitude requirements. This experiment, which we denote DREAM (dipolar recoupling enhanced by amplitude modulation) (*18*), is the first example of a homonuclear adiabatic polarization-transfer scheme that exploits double-quantum transitions. Homonuclear adiabatic zero-quantum mixing has been realized by an adiabatic passage through the rotational-resonance recoupling condition using spinning-frequency ramps (*19*) and is also conceivable in the rotating frame as implemented in the rotational-resonance tickling experiment (*20–22*). Adiabatic schemes have also found a number of applications as heteronuclear polarization-transfer schemes where different RF fields can be applied independently to the two coupled spins (*23–26*).

The DREAM sequence demonstrates the two well-known general advantages of adiabatic pulse schemes over their "sudden" equivalents: a more complete polarization transfer in powdered samples (theoretically an efficiency of 100% is obtained compared to a maximum of 73% for 'sudden' experiments for isolated spin-1/2 pairs) and robustness with respect to chemical-shift differences and experimental imperfections like RF-field inhomogeneity.

In this publication, we discuss the framework for a theoretical description of adiabatic homonuclear recoupling experiments. We use a Floquet approach (*27–32*) to deduce a time-independent Hilbert-space Hamiltonian using perturbation theory. The trajectory of the density operator during a DREAM period under the assumption of a fully adiabatic behavior is given and the theoretical models are verified experimentally. The broadbandedness of the DREAM sequence is improving with higher spinning frequency.

The performance of the DREAM recoupling sequence is described theoretically and measured experimentally for two

[1] To whom correspondence should be addressed. Fax: +41-1-632-1621. E-mail: beme@nmr.phys.chem.ethz.ch.

1090-7807/01 $35.00

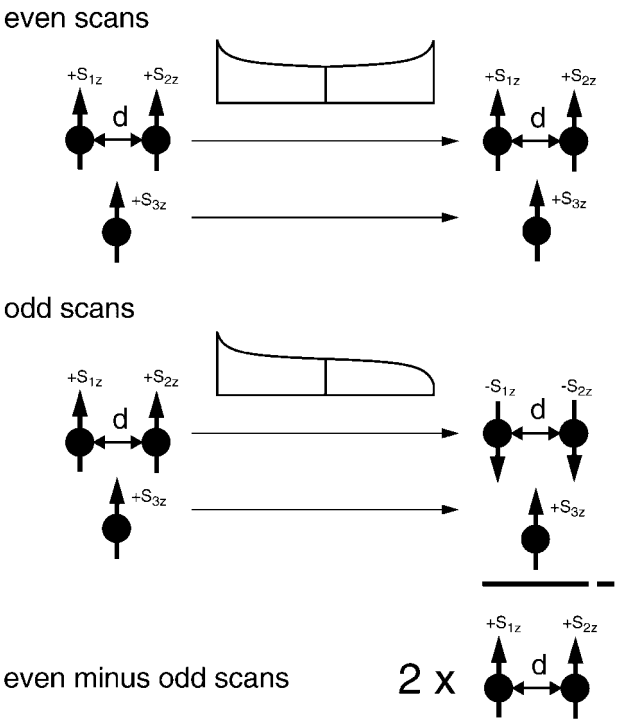

FIG. 1. Schematic representation of a DREAM spin-pair filter. The odd scans lead to an inversion of the magnetization of coupled spin pairs while they do not change the magnetization of uncoupled spins. The even scans leave coupled and uncoupled spins invariant. The difference of the two experiments yields a spectrum that contains only signals from the coupled spins. One could also add the two scans to select the signals from the uncoupled spins only.

different applications: in the context of spin-pair filtering and in the context of two-dimensional correlation spectroscopy as a mixing sequence. Two-spin filters (e.g., double-quantum filters) are useful to suppress the natural-abundance background signals in partially labeled materials (*2, 9, 33, 34*). Such suppression schemes are particularly important if labeled domains of a large biomolecule are investigated where the natural-abundance background of the rest of the molecule obscures the unfiltered spectrum (*35*). The principle of spin-pair filtering using adiabatic sweeps (*18*) is illustrated in Fig. 1. In the context of two-dimensional correlation spectroscopy, the DREAM sequence leads, for a spin pair, to a spectrum where all intensity is found in the cross peaks. The cross peaks have negative intensity because an adiabatic double-quantum process is applied. This concept is schematically illustrated in Fig. 2.

2. THEORETICAL DESCRIPTION

2.1. The Hamiltonian

We consider a system of N homonuclear spins, $\mathbf{S}_k$, with a spin-quantum number of 1/2. It is assumed that all other nuclei (heteronuclei) can be efficiently decoupled. During the DREAM period of an experiment, e.g., in a correlation experiment (Fig. 3a) or in a two-spin-filter experiment (Fig. 3b), an amplitude-modulated cw radiofrequency irradiation is applied to the spins. The Hamiltonian in the usual rotating frame which rotates with the Zeeman frequency about the external magnetic field B_0 contains the chemical shift $\mathcal{H}_{\mathrm{CS}}$, the dipolar interaction $\mathcal{H}_{\mathrm{d}}$, the homonuclear J-coupling $\mathcal{H}_J$, and the interaction of the spins with the applied RF field $\mathcal{H}_{\mathrm{RF}}$:

$$\mathcal{H}(t, T) = \mathcal{H}_{\mathrm{CS}}(t) + \mathcal{H}_{\mathrm{d}}(t) + \mathcal{H}_J + \mathcal{H}_{\mathrm{RF}}(T). \qquad [1]$$

The time dependences of the chemical shift and the dipolar interaction are caused by magic-angle sample spinning and are periodic with a cycle time of $\tau_{\mathrm{r}} = 2\pi/\omega_{\mathrm{r}}$, where $\omega_{\mathrm{r}}/(2\pi)$ is the MAS spinning frequency. The time-scale of the RF-amplitude variation is much slower than τ_{r} and we can assume that the amplitude of the RF irradiation, ω_1, is constant over a single rotor period. Therefore we denote the slow, parametric time dependence by a separate time variable, T (*36*).

The chemical-shift Hamiltonian can be written as the sum of an isotropic, $\mathcal{H}^0_{\mathrm{CS}}$, and an anisotropic, $\mathcal{H}^{\mathrm{a}}_{\mathrm{CS}}$, contribution:

$$\begin{aligned}\mathcal{H}_{\mathrm{CS}}(t) &= \mathcal{H}^0_{\mathrm{CS}} + \mathcal{H}^{\mathrm{a}}_{\mathrm{CS}}(t) \\ &= \sum_k \Omega^{(0)}_k S_{kz} + \sum_k \sum_{\substack{m=-2 \\ m\neq 0}}^{2} \Omega^{(m)}_k \exp(im\omega_{\mathrm{r}}t)\, S_{kz}. \qquad [2]\end{aligned}$$

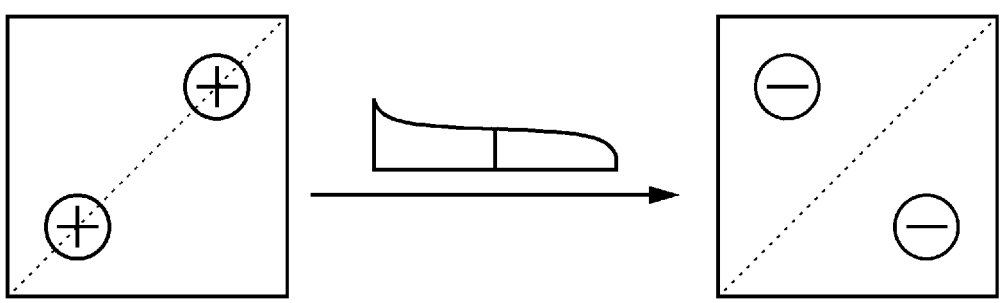

FIG. 2. Schematic representation of the use of a DREAM recoupling in the mixing time of a homonuclear shift-correlation spectrum for a coupled pair of spins. Without mixing, the two-dimensional spectrum has only diagonal peaks. The dipolar splitting is not resolved in the schematic spectrum shown. With a mixing time, all intensity is found in the cross peaks which have a negative signal intensity.

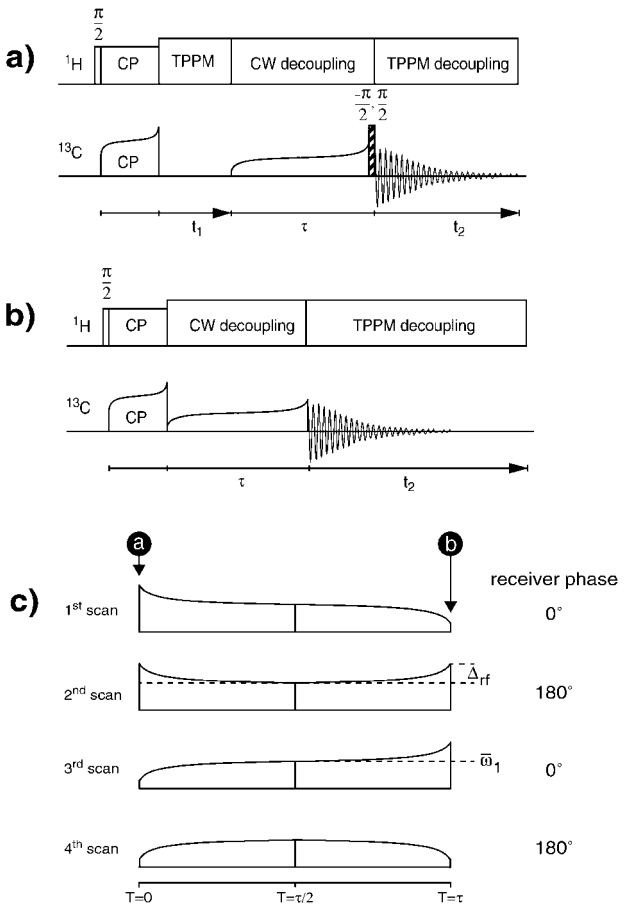

FIG. 3. Pulse sequence for (a) the two-dimensional DREAM correlation experiment and (b) the DREAM spin-pair selective experiments. (c) Four different amplitude shapes which can be used in the spin-pair filter experiment and appropriate modification of the receiver phase.

The Fourier coefficients of the anisotropic chemical-shift contribution ($\Omega_k^{(m)}$) are listed in the Appendix. The dipolar Hamiltonian is given by

$$\mathcal{H}_{\rm d}(t) = \sum_{k<\ell} d_{k\ell}(t)\left(2S_{kz}S_{\ell z} - \frac{1}{2}(S_k^+ S_\ell^- + S_k^- S_\ell^+)\right), \quad [3]$$

where $d_{k\ell}(t) = \sum_{m=\pm2,\pm1} d_{k\ell}^{(m)} e^{im\omega_r t}$ has no time-independent contribution. The Fourier coefficients $d_{k\ell}^{(m)}$ are also listed in the Appendix. The J-coupling is assumed to be isotropic:

$$\mathcal{H}_J = 2\pi \sum_{k<\ell} J_{k\ell}(\mathbf{S}_k \cdot \mathbf{S}_\ell). \quad [4]$$

The anisotropic contributions of the J-coupling can be included into $\mathcal{H}_{\rm d}$. The last term of Eq. [1] is the interaction of the spins with the RF field which is chosen to be along the x-axis of the rotating frame and is given by

$$\mathcal{H}_{\rm RF}(T) = \omega_1(T) \sum_k S_{kx}. \quad [5]$$

For the following discussion, it is convenient to write $\mathcal{H}(t, T)$ in a tilted coordinate system where the z-axis is aligned with the effective-field direction (averaged over a rotor period) for each single spin. The average effective-field direction is given by

$$\frac{\Omega_k^{(0)}}{\omega_{{\rm eff},\,k}(T)} S_{kz} + \frac{\omega_1(T)}{\omega_{{\rm eff},\,k}(T)} S_{kx}, \quad [6]$$

and the effective-field strength is defined as $\omega_{{\rm eff},\,k}(T) = \pm\sqrt{(\Omega_k^{(0)})^2 + (\omega_1(T))^2}$, where the sign of the square root is negative for a positive gyromagnetic ratio of the nuclei under consideration. The corresponding transformation into the tilted frame of reference can be described by a rotation operator $R(T) = \pi_k \exp(i\vartheta_k(T)S_{ky})$, where the tilt angle of the effective field of spin k is defined as $\vartheta_k(T) = \arctan(\omega_1(T)/\Omega_k^{(0)})$. The tilted system Hamiltonian $\tilde{\mathcal{H}}(t, T) = R(T)\mathcal{H}(t, T)R^\dagger(T)$ is given by

$$\tilde{\mathcal{H}}(t, T) = \tilde{\mathcal{H}}_{\rm eff}(T) + \tilde{\mathcal{H}}_{\rm CS}^{\rm a}(t, T) + \tilde{\mathcal{H}}_{\rm d}(t, T) + \tilde{\mathcal{H}}_J(T) \quad [7]$$

with

$$\tilde{\mathcal{H}}_{\rm eff}(T) = \tilde{\mathcal{H}}_{\rm CS}^0(T) + \tilde{\mathcal{H}}_{\rm RF}(T) = \sum_k \omega_{{\rm eff},\,k}(T) S_{kz}, \quad [8]$$

$$\tilde{\mathcal{H}}_{\rm CS}^{\rm a}(t, T) = \sum_k \Omega_k^{\rm a}(t)\cos(\vartheta_k(T))S_{kz} + \sum_k \Omega_k^{\rm a}(t)\sin(\vartheta_k(T))S_{kx}, \quad [9]$$

and

$$\begin{aligned}\tilde{\mathcal{H}}_{\rm d}(t, T) = \sum_{k<\ell} d_{k\ell}(t)\Big\{ & A_{k\ell}^{\rm d}(T)S_{kz}S_{\ell z} + B_{k\ell}^{\rm d}(T)\frac{1}{2} \\ & \times (S_k^+ S_\ell^- + S_k^- S_\ell^+) + R_{k\ell}^{\rm d}(T)(S_{kz}S_\ell^+ + S_{kz}S_\ell^-) \\ & + V_{k\ell}^{\rm d}(T)(S_k^+ S_{\ell z} + S_k^- S_{\ell z}) + Q_{k\ell}^{\rm d}(T)\frac{1}{2} \\ & \times (S_k^+ S_\ell^+ + S_k^- S_\ell^-)\Big\}. \end{aligned} \quad [10]$$

The coefficients $A_{k\ell}^{\rm d}(T)$, $B_{k\ell}^{\rm d}(T)$, $R_{k\ell}^{\rm d}(T)$, $V_{k\ell}^{\rm d}(T)$, and $Q_{k\ell}^{\rm d}(T)$ are listed in the Appendix. The J-coupling term in the tilted frame is given by

$$\begin{aligned}\tilde{\mathcal{H}}_J(T) = \sum_{k<\ell} \pi J_{k\ell}\Big\{ & A_{k\ell}^J(T)2S_{kz}S_{\ell z} + B_{k\ell}^J(T)\frac{1}{2} \\ & \times (S_k^+ S_\ell^- + S_k^- S_\ell^+) + R_{k\ell}^J(T)(S_{kz}S_\ell^+ + S_{kz}S_\ell^-) \\ & + V_{k\ell}^J(T)(S_k^+ S_{\ell z} + S_k^- S_{\ell z}) + Q_{k\ell}^J(T)\frac{1}{2} \\ & \times (S_k^+ S_\ell^+ + S_k^- S_\ell^-)\Big\} \end{aligned} \quad [11]$$

and the coefficients $A^J_{k\ell}(T)$, $B^J_{k\ell}(T)$, $R^J_{k\ell}(T)$, $V^J_{k\ell}(T)$, and $Q^J_{k\ell}(T)$ can also be found in the Appendix. We can express the entire time-dependent Hamiltonian $\tilde{\mathcal{H}}(t, T)$ in a Fourier series as

$$\tilde{\mathcal{H}}(t, T) = \sum_{n=-2}^{2} \tilde{\mathcal{H}}^{(n)}(T) \cdot e^{in\omega_r t}, \qquad [12]$$

where the $\tilde{\mathcal{H}}^{(n)}(T)$ are the Fourier coefficients of the Hamiltonian. The terms of Eq. [12] are composed of the terms of Eqs. [8] to [11] grouped by their respective time dependence.

If we denote the spin states of each spin as $|\alpha\rangle$ and $|\beta\rangle$ according to their polarization with respect to the effective quantization direction defined by $\tilde{\mathcal{H}}_{\text{eff}}$, the dipolar and J interactions can induce zero-quantum transitions (coefficient B), single-quantum transitions (coefficients R and V), and double-quantum transitions (coefficient Q).

All dipolar terms are t-time dependent and they will only significantly influence the spectrum at special recoupling conditions which occur during the slow RF amplitude variation for certain ratios of the RF-field strength and the spinning frequency.

The J-interaction term, on the other hand, is t-time independent and is able to influence the dynamics of the spin system at arbitrary ratios of MAS spinning frequency and RF-field strength. We will discuss later in this publication that the J-interaction does not play a significant role in practical applications.

The chemical-shift anisotropy can induce single-quantum transitions due to the second term of Eq. [9]. In addition, it modulates the energy levels of the $|\alpha\rangle$ and $|\beta\rangle$ states of each spin through the first term of Eq. [9]. The consequences of this modulation will be discussed below.

2.2. Floquet Description

To discuss the spin dynamics, it is beneficial to replace the time-dependent Hamiltonian $\tilde{\mathcal{H}}(t, T)$ by one that is t-time independent. For simplicity, we will treat only two-spin systems in this chapter. Nevertheless, we will keep the general notation where we denote one spin by k and the other by ℓ, because it is easy to generalize the Hamiltonian for a many-spin system. The calculation of the trajectory of the density operator, however, may become quite demanding in a many-spin system.

For stroboscopic observation, an average Hamiltonian description could be chosen with respect to the fast time scale (t) and the DREAM experiment can indeed be described by average Hamiltonian theory (*18*). Here, we choose the more general Floquet approach and we define a Floquet Hamiltonian $\tilde{\mathcal{H}}^{\text{F}}(T)$ that is only time dependent on the slow time scale of T. The Floquet description does not require an *a priori* choice of a particular interaction frame to properly describe the recoupling condition (*31*). The Floquet-space basis functions $|\phi, n\rangle$ are obtained from the Hilbert-space basis functions $|\phi\rangle$ by dressing with a Fourier coefficient n that runs from $-\infty$ to ∞ (*27*). For numerical applications, the range of n can be truncated. This is, however, not necessary in the present context. A schematic matrix representation of $\tilde{\mathcal{H}}^{\text{F}}(T)$ is shown in Fig. 4. The matrix elements are defined as

$$\langle \nu, m|\tilde{\mathcal{H}}^{\text{F}}(T)|\mu, n\rangle = \langle \nu|\tilde{\mathcal{H}}^{(n-m)}(T)|\mu\rangle + n\omega_r\delta_{mn}\delta_{\nu\mu}, \qquad [13]$$

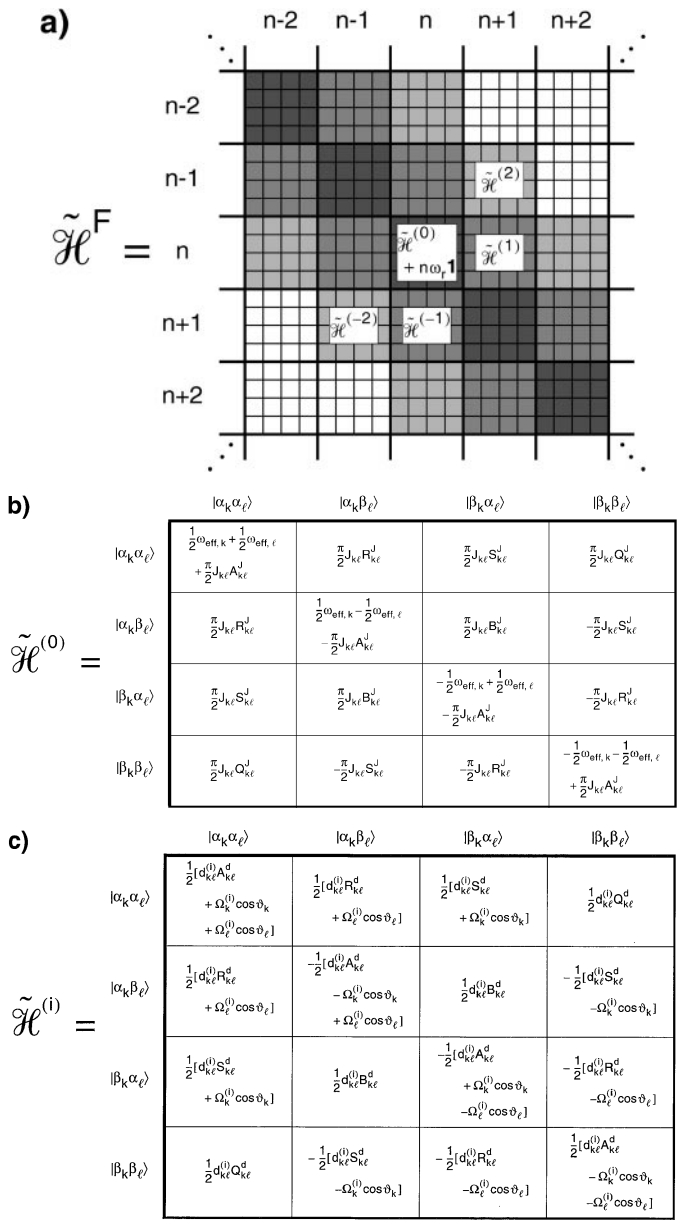

FIG. 4. Matrix representation of the Floquet Hamiltonian. (a) Schematic drawing indicating the different subblocks defined by the Fourier indices. The **1** represents the unity operator. (b) Explicit matrix elements of the Hamiltonian $\tilde{\mathcal{H}}^{(0)}$ correspondings to the subblock with the Fourier index zero on the main diagonal of the full Floquet matrix without the $n\omega_r$ **1** contribution. The elements contain contributions from the effective field and from the J-coupling. (c) Explicit matrix elements of the Hamiltonian $\tilde{\mathcal{H}}^{(i)}$ corresponding to the subblocks with the Fourier indices $i = \{-2, -1, 1, 2\}$ on the side diagonals of the full Floquet matrix. The elements contain contributions from the dipolar coupling and from the anisotropic part of the chemical shift.

based on the Fourier coefficients $\tilde{\mathcal{H}}^{(n)}(T)$ defined in Eq. [12]. These coefficients are given in Figs. 4b and 4c.

The standard way to solve the equation of motion involves the diagonalization of the Hamiltonian $\tilde{\mathcal{H}}^{\mathrm{F}}$. In the following, we use a perturbation treatment for approximate diagonalization (*37*) of the Floquet Hamiltonian. We divide the Floquet Hamiltonian into a dominant part $\tilde{\mathcal{H}}_0^{\mathrm{F}}$ and a perturbation part $\tilde{\mathcal{H}}_1^{\mathrm{F}}$. The dominant part $\tilde{\mathcal{H}}_0^{\mathrm{F}}$ describes the interaction with the mean effective field (Eq. [8]) and has the matrix elements

$$\langle \nu, n | \tilde{\mathcal{H}}_0^{\mathrm{F}}(T) | \mu, n \rangle = \langle \nu | \tilde{\mathcal{H}}_{\mathrm{eff}}(T) | \mu \rangle + n\omega_{\mathrm{r}}\delta_{\nu\mu}, \qquad [14]$$

while the perturbation $\tilde{\mathcal{H}}_1^{\mathrm{F}}$ contains all other terms and is defined as

$$\tilde{\mathcal{H}}_1^{\mathrm{F}}(T) = \tilde{\mathcal{H}}^{\mathrm{F}}(T) - \tilde{\mathcal{H}}_0^{\mathrm{F}}(T). \qquad [15]$$

The eigenvalues of the unperturbed Floquet Hamiltonian $\tilde{\mathcal{H}}_0^{\mathrm{F}}$ and, in zeroth-order perturbation theory, of $\tilde{\mathcal{H}}^{\mathrm{F}}$, are given by

$$\begin{aligned}
\langle \alpha_k\alpha_\ell, n | \tilde{\mathcal{H}}_0^{\mathrm{F}} | \alpha_k\alpha_\ell, n \rangle &= \frac{1}{2}(\omega_{\mathrm{eff},\,k} + \omega_{\mathrm{eff},\,\ell}) + n\omega_{\mathrm{r}} \\
\langle \alpha_k\beta_\ell, n | \tilde{\mathcal{H}}_0^{\mathrm{F}} | \alpha_k\beta_\ell, n \rangle &= \frac{1}{2}(\omega_{\mathrm{eff},\,k} - \omega_{\mathrm{eff},\,\ell}) + n\omega_{\mathrm{r}} \\
\langle \beta_k\alpha_\ell, n | \tilde{\mathcal{H}}_0^{\mathrm{F}} | \beta_k\alpha_\ell, n \rangle &= -\frac{1}{2}(\omega_{\mathrm{eff},\,k} - \omega_{\mathrm{eff},\,\ell}) + n\omega_{\mathrm{r}} \\
\langle \beta_k\beta_\ell, n | \tilde{\mathcal{H}}_0^{\mathrm{F}} | \beta_k\beta_\ell, n \rangle &= -\frac{1}{2}(\omega_{\mathrm{eff},\,k} + \omega_{\mathrm{eff},\,\ell}) + n\omega_{\mathrm{r}}.
\end{aligned} \qquad [16]$$

A numerical example for the eigenvalues as a function of the ratio between ω_1 and ω_{r} is shown in Fig. 5a. The variable T has been omitted in the above equation for simplicity of notation but all effective field strengths are T-time dependent. The matrix elements of the perturbation $\tilde{\mathcal{H}}_1^{\mathrm{F}}$ can be calculated from Eqs. [8]–[12].

It is obvious from the matrix elements of $\tilde{\mathcal{H}}^{(0)}(T)$ (Fig. 4b) that the diagonal blocks of the Floquet Hamiltonian $\tilde{\mathcal{H}}^{\mathrm{F}}$ contain additional elements which are not in $\tilde{\mathcal{H}}_0^{\mathrm{F}}$. These all originate from the *J*-coupling Hamiltonian and represent diagonal elements as well as off-diagonal elements in $\tilde{\mathcal{H}}^{(0)}(T)$.

We will neglect the small shift of the energy level caused by the *J*-coupling to the diagonal elements of $\tilde{\mathcal{H}}_1^{\mathrm{F}}$. The energy levels in first-order perturbation theory will only be changed if two states of $\tilde{\mathcal{H}}_0^{\mathrm{F}}$ connected by a matrix element of $\tilde{\mathcal{H}}_1^{\mathrm{F}}$ are close to degeneracy (*37*). From Eq. [16] we can see that the condition for degeneracy is

$$\omega_{\mathrm{eff},\,k} + \omega_{\mathrm{eff},\,\ell} = N \cdot \omega_{\mathrm{r}}, \qquad [17]$$

where the integer $N = -1, -2$ is limited by the number of side diagonals in $\tilde{\mathcal{H}}_1^{\mathrm{F}}$. The sign of N for the recoupling condition depends on the sign of the gyromagnetic ratio. Here and in the following we assume a positive gyromagnetic ratio, as is the case for carbon nuclei, and consequently a negative sign for the recoupling condition.

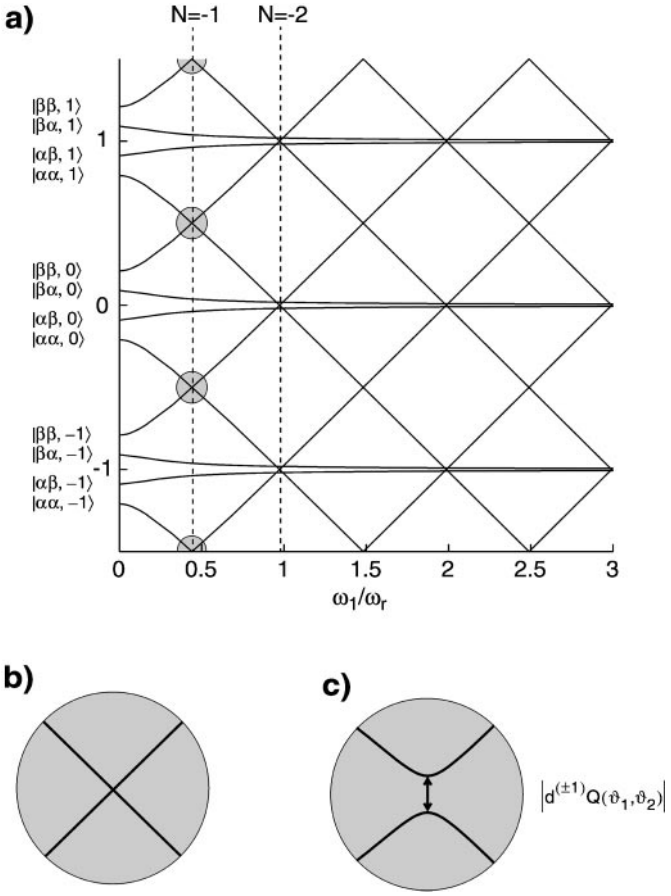

FIG. 5. (a) Energy-level diagram showing the eigenvalues of the Floquet matrix as a function of the RF-field strength in units of ω_{r}. The isotropic chemical shifts are set for this example to $0.3 \cdot \omega_{\mathrm{r}}$ and $0.125 \cdot \omega_{\mathrm{r}}$. The expanded areas in (b) and (c) show the level crossing in zeroth-order (b) and the avoided level crossing in first-order (c) perturbation theory for the $|\alpha_k\alpha_\ell, n\rangle$ and $|\beta_k\beta_\ell, n-1\rangle$ states around the generalized HORROR condition.

For the specific case of the HORROR condition, $N = -1$, the only pairwise degenerate states are $|\alpha_k\alpha_\ell, n\rangle$ and $|\beta_k\beta_\ell, n-1\rangle$. The first-order correction to the eigenvalues of $\tilde{\mathcal{H}}_0^{\mathrm{F}}$ is given by

$$\begin{aligned}
\langle \alpha_k\alpha_\ell, n | \tilde{\mathcal{H}}_1^{\mathrm{F}} | \beta_k\beta_\ell, n-1 \rangle &= \frac{1}{2} d_{k\ell}^{(+1)} Q_{k\ell}(T) \\
\langle \beta_k\beta_\ell, n-1 | \tilde{\mathcal{H}}_1^{\mathrm{F}} | \alpha_k\alpha_\ell, n \rangle &= \frac{1}{2} d_{k\ell}^{(-1)} Q_{k\ell}(T).
\end{aligned} \qquad [18]$$

This contribution lifts the degeneracy of the energy levels at the exact HORROR condition and leads to an avoided level crossing in the energy-level diagram (see Fig. 5c). The level splitting at the HORROR condition is simply given by the magnitude

of the relevant Fourier component of the dipolar coupling (see Appendix), scaled by the geometric factor $Q_{k\ell}(T)$.

At the second resonance condition, $N = -2$, four energy levels of $\tilde{\mathcal{H}}_0^{\mathrm{F}}$ become approximately degenerate (see Fig. 5a) and the relevant subspace is spanned by the (unperturbed) state functions $|\alpha\alpha, n\rangle, |\alpha\beta, n-1\rangle, |\beta\alpha, n-1\rangle$, and $|\beta\beta, n-2\rangle$. The relevant matrix elements at the $N = -2$ recoupling can be found in Fig. 4. The $N = -2$ resonance condition has been exploited in the mixed single-quantum and double-quantum (MSD) HORROR experiment (*38*) and will not be discussed here.

Avoided level crossings at $|N| > 2$ appear in higher-order perturbation theory in the presence of CSA tensors. Instead of calculating higher-order perturbation contributions, one can also include the CSA terms, which are proportional to S_{kz} (leading term of Eq. [9]), into the zeroth-order Hamiltonian $\tilde{\mathcal{H}}_0^{\mathrm{F}}$. In this case, $\tilde{\mathcal{H}}_0^{\mathrm{F}}$ is no longer diagonal but has a side-diagonal structure. Such an operator can be analytically diagonalized (*29, 39–41*), leading to $\tilde{\mathcal{H}}_0^{\mathrm{F}}$. The remaining perturbation in the dashed coordinate system $\tilde{\mathcal{H}}_1^{\prime\mathrm{F}}$ is obtained in full analogy to the treatment described in the literature (*29, 39–41*). The perturbation $\tilde{\mathcal{H}}_1^{\prime\mathrm{F}}$ contains dipolar-coupling elements on all side diagonals. Therefore, first-order perturbation theory in this frame will immediately lead to the higher resonance conditions for $|N| > 2$. With increasing $|N|$, however, the matrix elements decrease rapidly in size. The appearance of higher-order resonance conditions leads to some decrease of the dipolar coupling elements for the $|N| = 1, 2$ condition.

For the $N = -1$ HORROR condition we can truncate the size of the Floquet matrix by retaining only terms in the Floquet Hamiltonian that influence the energy in first-order perturbation theory. Combining Eqs. [16] and [18], we obtain the relevant matrix elements

$$\begin{aligned}
\langle \alpha_k\alpha_\ell, n|\tilde{\mathcal{H}}^{\mathrm{F}}|\alpha_k\alpha_\ell, n\rangle &= \frac{1}{2}(\omega_{\mathrm{eff},k}(T) + \omega_{\mathrm{eff},\ell}(T)) + n\omega_{\mathrm{r}} \\
\langle \beta_k\beta_\ell, n-1|\tilde{\mathcal{H}}^{\mathrm{F}}|\beta_k\beta_\ell, n-1\rangle & \\
= -\frac{1}{2}(\omega_{\mathrm{eff},k}(T) + \omega_{\mathrm{eff},\ell}(T)) &+ (n-1)\omega_{\mathrm{r}} \\
\langle \alpha_k\beta_\ell, n|\tilde{\mathcal{H}}^{\mathrm{F}}|\alpha_k\beta_\ell, n\rangle &= \frac{1}{2}(\omega_{\mathrm{eff},k}(T) - \omega_{\mathrm{eff},\ell}(T)) + n\omega_{\mathrm{r}}. \qquad [19] \\
\langle \beta_k\alpha_\ell, n|\tilde{\mathcal{H}}^{\mathrm{F}}|\beta_k\alpha_\ell, n\rangle &= -\frac{1}{2}(\omega_{\mathrm{eff},k}(T) - \omega_{\mathrm{eff},\ell}(T)) + n\omega_{\mathrm{r}} \\
\langle \alpha_k\alpha_\ell, n|\tilde{\mathcal{H}}^{\mathrm{F}}|\beta_k\beta_\ell, n-1\rangle &= \frac{1}{2}d_{k\ell}^{(+1)}Q_{k\ell}(T) \\
\langle \beta_k\beta_\ell, n-1|\tilde{\mathcal{H}}^{\mathrm{F}}|\alpha_k\alpha_\ell, n\rangle &= \frac{1}{2}d_{k\ell}^{(-1)}Q_{k\ell}(T).
\end{aligned}$$

As mentioned earlier, the off-diagonal terms of the J-coupling in $\tilde{\mathcal{H}}^{(0)}(T)$ can lead to a mixing between the $|\alpha_k\beta_\ell, n\rangle$ and $|\beta_k\alpha_\ell, n\rangle$ states through the zero-quantum term of the J-coupling $\pi J_{k\ell}B_{k\ell}^J(T)\frac{1}{2}(S_k^+S_\ell^- + S_k^-S_\ell^+)$. This mixing is independent of the ratio between ω_{r} and ω_1 but requires that the effective-field difference is smaller than the J-coupling, i.e., $|\frac{1}{2}\omega_{\mathrm{eff},k} - \frac{1}{2}\omega_{\mathrm{eff},\ell}| \lesssim |2\pi J|$. For ^{13}C or ^{15}N spectroscopy, the J-couplings are usually small enough that this effect can be neglected except if the RF carrier is placed in the middle between two resonances (within the magnitude of J) or if the two resonances are almost degenerate. In practical applications, this is rarely of relevance and will not be discussed further.

We can now make the substitution $\omega_{\mathrm{eff},k}(T) = \bar{\omega}_k + \Delta_k(T)$ where $\bar{\omega}_k$ is the effective field of spin k at the HORROR condition and $\Delta_k(T)$ is the time-dependent deviation from this resonance condition due to an amplitude modulation of the RF field. For a spin pair, the matrix representation of the Floquet Hamiltonian of Eq. [19] can be written as the direct sum of (infinitely many) two-by-two matrices H_n^Σ and H_n^Δ. We define a double-quantum operator, $\tilde{\mathcal{H}}^\Sigma$, which has the matrix representation

$$\begin{aligned}
\mathrm{H}_n^\Sigma(T) = &\begin{bmatrix} \frac{1}{2}(\Delta_k(T) + \Delta_\ell(T)) & \frac{1}{2}d_{k\ell}^{(+1)}Q_{k\ell}(T) \\ \frac{1}{2}d_{k\ell}^{(-1)}Q_{k\ell}(T) & -\frac{1}{2}(\Delta_k(T) + \Delta_\ell(T)) \end{bmatrix} \\
&+ \left(n - \frac{1}{2}\right)\omega_{\mathrm{r}}\begin{bmatrix} 1 & 0 \\ 0 & 1 \end{bmatrix} \qquad [20]
\end{aligned}$$

in a basis spanned by $|\alpha_k\alpha_\ell, n\rangle$ and $|\beta_k\beta_\ell, n-1\rangle$. The part proportional to the identity matrix can be discarded. Defining the usual pseudo spin-1/2 operators (*42, 43*) and denoting them S_x^Σ, S_y^Σ, and S_z^Σ, Eq. [20] can be written in operator form as

$$\begin{aligned}
\tilde{\mathcal{H}}^\Sigma(T) = &(\Delta_k(T) + \Delta_\ell(T))S_z^\Sigma \\
&- d'_{k\ell}(T)\big(\cos(\varphi_{k\ell})S_x^\Sigma - \sin(\varphi_{k\ell})S_y^\Sigma\big). \qquad [21]
\end{aligned}$$

Here, the substitution

$$d'_{k\ell}(T) = \frac{d_{k\ell}}{2\sqrt{2}}Q_{k\ell}(T)\sin\left(2\theta_k^\ell\right) \qquad [22]$$

was used together with Eq. [A-2] in the Appendix. The same result has also been obtained by average Hamiltonian theory (*18*). For simplicity, this Hamiltonian can be rotated by $\varphi_{k\ell}$ around S_z^Σ to obtain the form

$$\tilde{\mathcal{H}}^\Sigma(T) = (\Delta_k(T) + \Delta_\ell(T))S_z^\Sigma - d'_{k\ell}(T)S_x^\Sigma. \qquad [23]$$

In a basis spanned by $|\alpha_k\beta_\ell, n\rangle$ and $|\beta_k\alpha_\ell, n\rangle$, the corresponding zero-quantum operator $\tilde{\mathcal{H}}_n^\Delta$ has the matrix representation

$$\begin{aligned}
\mathrm{H}_n^\Delta(T) = &\begin{bmatrix} \frac{1}{2}(\Delta_k(T) - \Delta_\ell(T)) & 0 \\ 0 & -\frac{1}{2}(\Delta_k(T) - \Delta_\ell(T)) \end{bmatrix} \\
&+ n\omega_{\mathrm{r}}\begin{bmatrix} 1 & 0 \\ 0 & 1 \end{bmatrix}. \qquad [24]
\end{aligned}$$

The operator form of the corresponding Hilbert-space Hamiltonian, dropping the terms proportional to the unity operator, is given by

$$\tilde{\mathcal{H}}^{\Delta}(T) = (\Delta_k(T) - \Delta_\ell(T))S_z^{\Delta}. \quad [25]$$

Such a zero-quantum operator does not lead to a time evolution of an initial density operator which is diagonal in this basis. Therefore, the zero-quantum polarization does not evolve during the DREAM period as long as the J-coupling is not active.

The Floquet numbers do not influence the NMR observables. Consequently, the time evolution can be described by a t-time-independent Hilbert-space Hamiltonian which is given by the direct sum of the double-quantum Hamiltonian (Eq. [23]) and the zero-quantum Hamiltonian (Eq. [25]),

$$\begin{aligned}\tilde{\mathcal{H}}(T) &= \tilde{\mathcal{H}}^{\Sigma}(T) \oplus \tilde{\mathcal{H}}^{\Delta}(T) = (\Delta_k(T) + \Delta_\ell(T))S_z^{\Sigma} \\ &\quad + (\Delta_k(T) - \Delta_\ell(T))S_z^{\Delta} - d'_{k\ell}(T)S_x^{\Sigma} \\ &= \Delta_k(T)S_{kz} + \Delta_\ell(T)S_{\ell z} - d'_{k\ell}(T)\frac{1}{2}(S_k^+ S_\ell^+ + S_k^- S_\ell^-). \end{aligned} \quad [26]$$

2.3. Amplitude Shape and Adiabaticity

The Hamiltonian of Eq. [26], which was derived in the framework of first-order perturbation theory, describes a passage through the $N = -1$ HORROR condition by means of an amplitude variation of the applied RF field. This passage is adiabatic if

$$a_{k\ell}(T) = \frac{\sqrt{(\Delta_k(T) + \Delta_\ell(T))^2 + (d'_{k\ell}(T))^2}}{|d\Theta_{k\ell}(T)/dT|} \gg 1. \quad [27]$$

Note that in general the adiabaticity parameter, $a_{k\ell}(T)$, will change over the course of the sweep. Furthermore, it depends on the crystallite orientation. Constant adiabaticity sweeps are only possible for a single two-spin system in a single orientation (*44*, *45*). Equation [27] is based on the simplified Hamiltonian of Equation [23] and $\Theta_{k\ell}(T)$ denotes the angle between the Hamiltonian and the z-axis of the double-quantum subspace

$$\Theta_{k\ell}(T) = \arctan\left(\frac{d'_{k\ell}(T)}{\Delta_k(T) + \Delta_\ell(T)}\right). \quad [28]$$

Here, $\Theta_{kl}(T)$ is always chosen between 0 and π. A tangential variation of the RF amplitude is schematically shown in Fig. 3,

$$\omega_1(T) = \bar{\omega}_1 + d_{\text{est}} \tan\left(\alpha \cdot \left(\frac{1}{2}\tau - T\right)\right), \quad [29]$$

with $\alpha = \frac{2}{\tau}\arctan(\frac{\Delta_{\text{RF}}}{d_{\text{est}}})$. Here, d_{est} and Δ_{RF} are experimental parameters and d_{est} should be close to the expected value of the dipolar coupling $d'_{k\ell}(T)$. Because this value depends on the crystallite orientation, a compromise has to be chosen. The tangential variation of Eq. [29] will, approximately, correspond to a theoretical adiabatic variation around the HORROR condition,

$$\Delta_k(T) + \Delta_\ell(T) = d'_{k\ell}(T) \tan\left(\alpha_{k\ell} \cdot \left(\frac{1}{2}\tau - T\right)\right), \quad [30]$$

with constant angular velocity $\alpha_{k\ell} = d\Theta_{k\ell}(T)/dT$ if the sweep is centered around the HORROR condition, $\bar{\omega}_1$. The T-time dependence of $d'_{k\ell}(T)$ (through $Q_{k\ell}(T)$, see Eq. [22]) is small if the amplitude of the applied RF field ω_1 exceeds the chemical-shift offset. Then, the identification $d_{\text{est}} \approx d'_{k\ell}(T = \tau/2)$ and $2\Delta_{\text{RF}} \approx \Delta_k(0) + \Delta_\ell(0)$ can be made. It should be noted, however, that the precise shape of $\omega_1(T)$ is not very important. In the absence of relaxation all amplitude shapes with an amplitude variation from $-\Delta_{\text{RF}}$ to Δ_{RF} are equivalent, as long as Condition [27] is fulfilled at all times T. In practical applications, the amplitude sweep should be as short as possible to minimize relaxation effects. A tangential variation is a reasonable compromise (*24*) between insensitivity to $d'_{k\ell}(T)$ and chemical-shift offsets and optimization of sweep time.

2.4. The Time Evolution of the Density Operator

In the following, we will discuss the evolution of the density operator during the DREAM period for a strongly coupled spin pair and for uncoupled spins. We assume a fully adiabatic passage ($a_{k\ell} \to \infty$) through the HORROR condition for the spin pair. The discussion in this chapter is specific to two-spin systems and we replace the indices $\{k, \ell\}$ with $\{1, 2\}$.

2.4.1. Coupled spin pair. For an adiabatic sweep the part of the initial density operator $\tilde{\sigma}(0^-)$ that is proportional to the Hamiltonian at the start of the sweep ($T = 0$) remains parallel to the Hamiltonian until the end of the DREAM sweep. We assume that the components of the density operator that are orthogonal to $\tilde{\mathcal{H}}(0)$ decay during the sweep due to RF inhomogeneity or due to relaxation processes, or that they will be eliminated by an appropriate phase cycle. The density operator at the end of the DREAM period can, therefore, be calculated by the following two steps:

(i) Projecting the initial density operator $\tilde{\sigma}(0^-)$ onto the system Hamiltonian $\tilde{\mathcal{H}}(0)$ of Eq. [26] (in this and the following paragraphs we will use "$-$" and "$+$" superscripts to signify the times just before or just after a projection of the density operator).

$$\tilde{\sigma}(0^+) = c_1\tilde{\mathcal{H}}(0), \quad [31]$$

with

$$c_1 = \frac{\mathrm{Tr}\{\tilde{\sigma}(0^-)\cdot\tilde{\mathcal{H}}(0)\}}{\mathrm{Tr}\{\tilde{\mathcal{H}}(0)\cdot\tilde{\mathcal{H}}(0)\}}. \quad [32]$$

Using the pseudo spin-1/2 formalism introduced above, and the initial density operator $\sigma(0^-) = a_1 S_{1x} + a_2 S_{2x}$ in the laboratory frame, we obtain, in the tilted frame of reference,

$$\tilde{\sigma}(0^-) = a_1[\sin(\vartheta_1(0))S_{1z} + \cos(\vartheta_1(0))S_{1x}] + a_2[\sin(\vartheta_2(0))S_{2z} + \cos(\vartheta_2(0))S_{2x}], \quad [33]$$

where $\vartheta_k(T) = \arctan(\omega_1(T)/\Omega_k^{(0)})$ is the tilt angle introduced earlier. For strong fields (compared to the chemical-shift offset) $\vartheta_k(0)$ approaches $\frac{\pi}{2}$ for all nuclei k and the cosine terms approach zero. Equation [33] simplifies under this condition to $\tilde{\sigma}(0^-) = a_1 S_{1z} + a_2 S_{2z}$. The projection of the density operator onto the Hamiltonian (Eq. [26]) according to Eqs. [31] and [32] is performed in two steps. Because the full Hamiltonian of Eq. [26] can be written as the direct sum of the zero-quantum and the double-quantum Hamiltonian, we first project $\tilde{\sigma}(0^-)$ onto each of the two subspaces. This leads to the zero-quantum subspace contribution,

$$\tilde{\sigma}^{\Delta} = [a_1 \sin(\vartheta_1(0)) - a_2 \sin(\vartheta_2(0))]S_z^{\Delta}, \quad [34]$$

and to the double-quantum subspace contribution,

$$\tilde{\sigma}^{\Sigma} = [a_1 \sin(\vartheta_1(0)) + a_2 \sin(\vartheta_2(0))]S_z^{\Sigma}. \quad [35]$$

In a second step, the projection of $\tilde{\sigma}^{\Delta}$ and $\tilde{\sigma}^{\Sigma}$ onto the zero-quantum and double-quantum Hamiltonians of Eqs. [23] and [25] leads to

$$\tilde{\sigma}^{\Sigma}(0^+) = [a_1 \sin(\vartheta_1(0)) + a_2 \sin(\vartheta_2(0))]\cdot\cos(\Theta_{12}(0)) \times \left[\cos(\Theta_{12}(0))S_z^{\Sigma} + \sin(\Theta_{12}(0))S_x^{\Sigma}\right] \quad [36]$$

for the double-quantum subspace while the zero-quantum subspace is unchanged and results in

$$\tilde{\sigma}^{\Delta}(0^+) = [a_1 \sin(\vartheta_1(0)) - a_2 \sin(\vartheta_2(0))]S_z^{\Delta}. \quad [37]$$

Here, $\Theta_{12}(0)$ is the angle between the Hamiltonian $\tilde{\mathcal{H}}^{\Sigma}(0)$ and the z-axis of the double-quantum subspace (see Eq. [28]). If the spinning frequency is considerably larger than the dipolar coupling d'_{12}, we can always start the sweep far off the HORROR condition. Then, $\Theta_{12}(0)$ approaches zero and, for the ideal case with $\Theta_{12}(0) = 0$ and $\vartheta_1(0) = \vartheta_2(0) = \frac{\pi}{2}$, Eqs. [36] and [37] simplify to

$$\tilde{\sigma}^{\Sigma}(0^+) = (a_1 + a_2)S_z^{\Sigma}$$
$$\tilde{\sigma}^{\Delta}(0^+) = (a_1 - a_2)S_z^{\Delta}. \quad [38]$$

Equations [36] and [37] and their simplified version of Eq. [38] describe the relevant density operator at the beginning of the DREAM sweep.

(ii) Rotation of the density operator by the DREAM sweep. In the second step the density operator $\tilde{\sigma}$ follows the rotation of the Hamiltonian and always stays parallel to the Hamiltonian. At the end of the sweep,

$$\tilde{\sigma}(\tau^-) = c_2\tilde{\mathcal{H}}(\tau) \quad [39]$$

holds, leading to

$$\tilde{\sigma}^{\Sigma}(\tau^-) = [a_1 \sin(\vartheta_1(0)) + a_2 \sin(\vartheta_2(0))]\cdot\cos(\Theta_{12}(0)) \times \left[\cos(\Theta_{12}(\tau))S_z^{\Sigma} + \sin(\Theta_{12}(\tau))S_x^{\Sigma}\right] \quad [40]$$

and

$$\tilde{\sigma}^{\Delta}(\tau^-) = [a_1 \sin(\vartheta_1(0)) - a_2 \sin(\vartheta_2(0))]S_z^{\Delta}. \quad [41]$$

Here, $\Theta_{12}(\tau)$, the angle between $\tilde{\mathcal{H}}^{\Sigma}(\tau)$ and S_z^{Σ}, is defined as

$$\Theta_{12}(\tau) = \arctan\left(\frac{d'_{12}(\tau)}{\Delta_1(\tau) + \Delta_2(\tau)}\right). \quad [42]$$

The initial projection with $\Theta_{12}(0)$, the rotation, and the final projection with $\Theta_{12}(\tau)$ of the density in the double-quantum subspace are schematically shown in Fig. 6.

For the ideal case $\Theta_{12}(0) = 0, \Theta_{12}(\tau) = \pi$, and $\vartheta_1(0) = \vartheta_2(0) = \pi/2$ we obtain

$$\tilde{\sigma}^{\Sigma}(\tau^-) = -(a_1 + a_2)S_z^{\Sigma}$$
$$\tilde{\sigma}^{\Delta}(\tau^-) = (a_1 - a_2)S_z^{\Delta}. \quad [43]$$

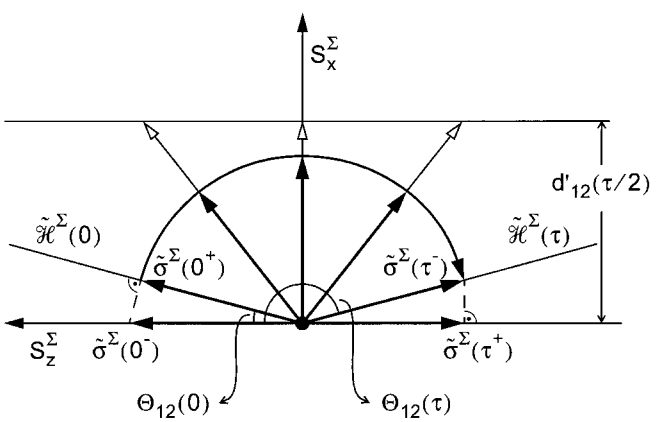

FIG. 6. Schematic representation of the initial projection with $\Theta_{12}(0)$, the subsequent rotation imposed by the rotation of the Hamiltonian, and final projection with $\Theta_{12}(\tau)$ of the the density operator in the double-quantum subspace.

In our application, the DREAM period is always followed by detection in the usual rotating frame. To obtain the density operator in this frame, $\sigma(\tau^+)$, we first transform back from the tilted frame to the rotating frame using the rotation matrix $R(\tau) = \pi_{k=1,2} \exp(i\vartheta_k(\tau)S_{ky})$ and then project onto the detection operators S_{1x} and S_{2x} to obtain the part of the density operator $\sigma(\tau^+)$ that contributes to the integrated signal intensity of the two resonances. The final density operator projected on these detection operators is given by

$$\sigma(\tau^+) = (a_{11} + a_{21})S_{1x} + (a_{22} + a_{12})S_{2x}, \qquad [44]$$

with

$$\begin{aligned}
a_{11} &= -\frac{1}{2}a_1 \sin(\vartheta_1(0)) \sin(\vartheta_1(\tau))[\cos(\Theta_{12}(0)) \cos(\Theta_{12}(\tau)) - 1] \\
a_{22} &= -\frac{1}{2}a_2 \sin(\vartheta_2(0)) \sin(\vartheta_2(\tau))[\cos(\Theta_{12}(0)) \cos(\Theta_{12}(\tau)) - 1] \\
a_{12} &= -\frac{1}{2}a_1 \sin(\vartheta_1(0)) \sin(\vartheta_2(\tau))[\cos(\Theta_{12}(0)) \cos(\Theta_{12}(\tau)) + 1] \\
a_{21} &= -\frac{1}{2}a_2 \sin(\vartheta_2(0)) \sin(\vartheta_1(\tau))[\cos(\Theta_{12}(0)) \cos(\Theta_{12}(\tau)) + 1].
\end{aligned} \qquad [45]$$

In the following, we will omit the "+" superscript on the time variable τ and denote the relevant part of the final density operator after the DREAM sequence by $\sigma(\tau)$. The four coefficients $a_{k\ell}$ denote the polarization (or coherence, depending on the frame of reference) transferred from spin k to ℓ during an adiabatic DREAM sweep. They can be directly mapped as cross peaks and diagonal peaks in a 2D correlation experiment. If the adiabatic sweep starts and ends far away from the HORROR condition (i.e., $\Theta_{12}(0) \approx 0$ and $\Theta_{12}(\tau) \approx \pi$) and relaxation processes can be neglected, no polarization remains on the source spin:

$$\begin{aligned}
a_{11} &\approx 0 \\
a_{22} &\approx 0 \\
a_{12} &\approx -a_1 \sin(\vartheta_1(0)) \sin(\vartheta_2(\tau)) \\
a_{21} &\approx -a_2 \sin(\vartheta_2(0)) \sin(\vartheta_1(\tau)).
\end{aligned} \qquad [46]$$

In practical applications for ^{15}N or ^{13}C nuclei, conditions where Eq. [46] is valid can easily be realized. The scaled dipolar coupling d'_{12}, which does not exceed 1 kHz, is smaller than the sum of the RF fields, $\Delta_1(0) + \Delta_2(0)$, and $\cos(\Theta_{12}(0)) \approx 1$.

If the chemical-shift offsets are small compared to the MAS frequency, a complete polarization exchange between the two spins takes place with

$$\begin{aligned}
a_{11} &= 0 \\
a_{22} &= 0 \\
a_{12} &= -a_1 \\
a_{21} &= -a_2
\end{aligned} \qquad [47]$$

and

$$\sigma(\tau) = -(a_2 S_{1x} + a_1 S_{2x}). \qquad [48]$$

The initial magnetization on spin 1 ends up on spin 2 and vice versa. This leads to a 2D spectrum, schematically shown in Fig. 2.

The terms $\sin(\vartheta_k(t))$ in Eq. [46] are a measure for the loss of magnetization during the experiment due to the projections described above and depend only on the ratio between RF-field strength, which is linked to the MAS frequency, and chemical-shift offset. For large chemical-shift offsets where the ideal situation of Eq. [48] is not fulfilled, it is obvious that in general $a_{12} \neq a_{21}$.

Figure 7 illustrates the contributions of the relevant factors to the transfer efficiencies a_{11}, a_{22}, a_{12}, and a_{21} described by Eq. [45] as a function of the frequency offset, i.e., the offset of the carrier frequency from the center between the two spins. The thick lines show the influence of the $\cos(\Theta_{12}(t))$ terms while the thin lines illustrate the influence of the $\sin(\vartheta_k(t))$ terms on the transfer efficiencies. It can clearly be seen that the $\cos(\Theta_{12}(t))$ term defines the window where transfer can take place while the $\sin(\vartheta_k(t))$ term determines the amount of transfer. The $\cos(\Theta_{12}(t))$ terms are related to the

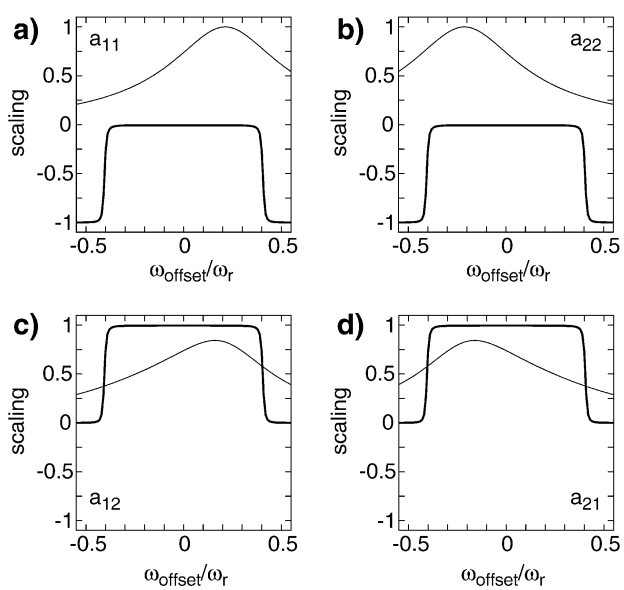

FIG. 7. Contributions to the transfer efficiencies (a) a_{11}, (b) a_{22}, (c) a_{12}, and (d) a_{21} described by Eq. [45] as a function of the frequency offset, i.e., the offset of the carrier frequency from the center between the two spins. The thick lines shows the influence of the $\cos(\Theta_{12}(t))$ terms while the thin lines illustrate the influence of the $\sin(\vartheta_{12}(t))$ terms on the transfer efficiencies. It can clearly be seen that the $\cos(\Theta_{12}(t))$ term determines whether we will see any transfer at all while the $\sin(\vartheta_{12}(t))$ term determines the amount of the transfer. A dipolar coupling constant of $d_{12} = 0.08 \cdot \omega_r$, an isotropic chemical-shift difference $\Omega_1^0 - \Omega_2^0 = 0.425\ \omega_r$, an average RF amplitude of $\bar{\omega}_1 = 0.445 \cdot \omega_r$, and an initial offset of $\Delta_{RF} = 0.18 \cdot \omega_r$ were used for the calculations.

TABLE 1
Scaling Factors for the Four Sweeps (Fig. 3c) in Coupled Spin Pairs and Isolated Spins

	Dipolar coupled				Isolated
	a_{11}	a_{22}	a_{12}	a_{21}	a_{kk}
First scan	0	0	$-a_1 \sin(\vartheta_1^{\mathrm{a}}) \sin(\vartheta_2^{\mathrm{b}})$	$-a_2 \sin(\vartheta_2^{\mathrm{a}}) \sin(\vartheta_1^{\mathrm{b}})$	$a_k \sin(\vartheta_k^{\mathrm{a}}) \sin(\vartheta_k^{\mathrm{b}})$
Second scan	$a_1 \sin^2(\vartheta_1^{\mathrm{a}})$	$a_2 \sin^2(\vartheta_2^{\mathrm{a}})$	0	0	$a_k \sin^2(\vartheta_k^{\mathrm{a}})$
Third scan	0	0	$-a_1 \sin(\vartheta_1^{\mathrm{b}}) \sin(\vartheta_2^{\mathrm{a}})$	$-a_2 \sin(\vartheta_2^{\mathrm{b}}) \sin(\vartheta_1^{\mathrm{a}})$	$a_k \sin(\vartheta_k^{\mathrm{b}}) \sin(\vartheta_k^{\mathrm{a}})$
Fourth scan	$a_1 \sin^2(\vartheta_1^{\mathrm{b}})$	$a_2 \sin^2(\vartheta_2^{\mathrm{b}})$	0	0	$a_k \sin^2(\vartheta_k^{\mathrm{b}})$

trajectory the density operator traces out in the double-quantum subspace. The quenching of all transfer outside the sharply defined $\cos(\Theta_{12}(t))$ window is caused by the fact that the spins never go through the HORROR condition outside this window. At the edge of the window, we have $\Theta_{12}(t) = \pi/2$. The terms containing $\sin(\vartheta_1(t))$ and/or $\sin(\vartheta_2(t))$ are only related to the projection of the density operator onto the effective field. The window of transfer can be enlarged by choosing a large value for Δ_{RF}. However this implies that either at the start or at the end of the sweep the amplitude of the RF field will be smaller and that the scaling caused by the terms dependent on $\sin(\vartheta_1(t))$ and/or $\sin(\vartheta_2(t))$ may become more severe. In an actual experiment, the product of both contributions will be observed.

The coefficients of Eqs. [45] have been evaluated for all four amplitude shapes shown in Fig. 3c. The angles $\vartheta_k(0)$ and $\vartheta_k(\tau)$ in any of the four scans can be expressed by the initial and final angles of the first scan of Fig. 3c, which we denote by ϑ_k^{a} and ϑ_k^{b}, respectively. For example, for the first scan $\vartheta_k(0) = \vartheta_k^{\mathrm{a}}$ and $\vartheta_k(\tau) = \vartheta_k^{\mathrm{b}}$, while for the second scan $\vartheta_k(0) = \vartheta_k(\tau) = \vartheta_k^{\mathrm{a}}$. The transfer efficiencies for the four shapes are given in Table 1.

2.4.2. Uncoupled spins. For isolated spins, no polarization transfer takes place. In two-dimensional spectra, all signals from isolated spins stay on the diagonal. The density operator, $\sigma(\tau)$, is evaluated by taking into account the projection of the initial density operator onto the Hamiltonian (which consists of chemical-shift and RF terms) at the beginning of the sweep and back onto the detection operator at time τ. One obtains

$$\sigma(\tau) = \sum_k a_{kk} S_{kx}. \qquad [49]$$

The value of the coefficient a_{kk} is given, for the four shape variations of Fig. 3c, in Table 1. For small chemical-shift offsets $\vartheta_k(\tau) \to 0$, the signal intensity is not influenced by the DREAM sweep at all.

$$\sigma(0) = \sigma(\tau) = \sum_k a_k S_{kx} \qquad [50]$$

2.4.3. Shape cycles. The effect of finite chemical-shift offsets as expressed by the angle $\vartheta_k < \pi/2$ on the peak intensities in a two-dimensional correlation experiment consists only of intensity variations for the cross peaks. The influence decreases with increasing spinning frequency because the applied RF-field strength at the center of the DREAM sweep is equal to half the spinning frequency. For spinning frequencies, which are large compared to isotropic chemical-shift differences, the influence of the chemical-shift offset is, therefore, rather minor.

In spin-pair filtering experiments, however, these influences are more pronounced because the experiment requires a good suppression of the uncoupled (or very weakly coupled) spins. The shortest shape cycle consist of two shapes, namely the first and second ones shown in Fig. 3c. From Table 1 we obtain the following coefficients for the signal intensity of an isolated spin,

$$a_k \sin(\vartheta_k^{\mathrm{a}}) \left[\sin(\vartheta_k^{\mathrm{a}}) - \sin(\vartheta_k^{\mathrm{b}}) \right]. \qquad [51]$$

The experiments in which four shapes are combined have advantages for the suppression of uncoupled spins. The combination of all four shapes for an isolated spin leads according to Table 1 to

$$a_k \left[\sin(\vartheta_k^{\mathrm{a}}) - \sin(\vartheta_k^{\mathrm{b}}) \right]^2. \qquad [52]$$

For angles around $\vartheta_k^{\mathrm{a}} \approx \vartheta_k^{\mathrm{b}} \approx \pi/2$ or $\sin(\vartheta_k^{\mathrm{a}}) \approx \sin(\vartheta_k^{\mathrm{b}}) \approx 1$, the better suppression behavior of the four-sweep version can easily be seen from the fact that $\varepsilon^2 < \varepsilon$ for $\varepsilon = \sin(\vartheta_k^{\mathrm{a}}) - \sin(\vartheta_k^{\mathrm{b}}) \ll 1$.

For a particular choice of chemical-shift offsets the filter efficiency for spin pairs (Figs. 8a–8c) and for isolated spins (Figs. 8d–8f) in a spin-pair filter experiment are shown as a function of the carrier offset ω_{offset} which is referenced to the center frequency of the two spins. Figure 8a shows the filter efficiency of the sum magnetization of a coupled spin pair, while Figs. 8b and 8c show the efficiencies for the two spins separately. Figure 8d shows the filter efficiency of the sum magnetization for two uncoupled spins while Figs. 8e and 8f show the two spins separately. More details of the simulation can be found in the figure legend. The thick lines shows the results for the combination of all four experiments of Fig. 3c. The dashed and

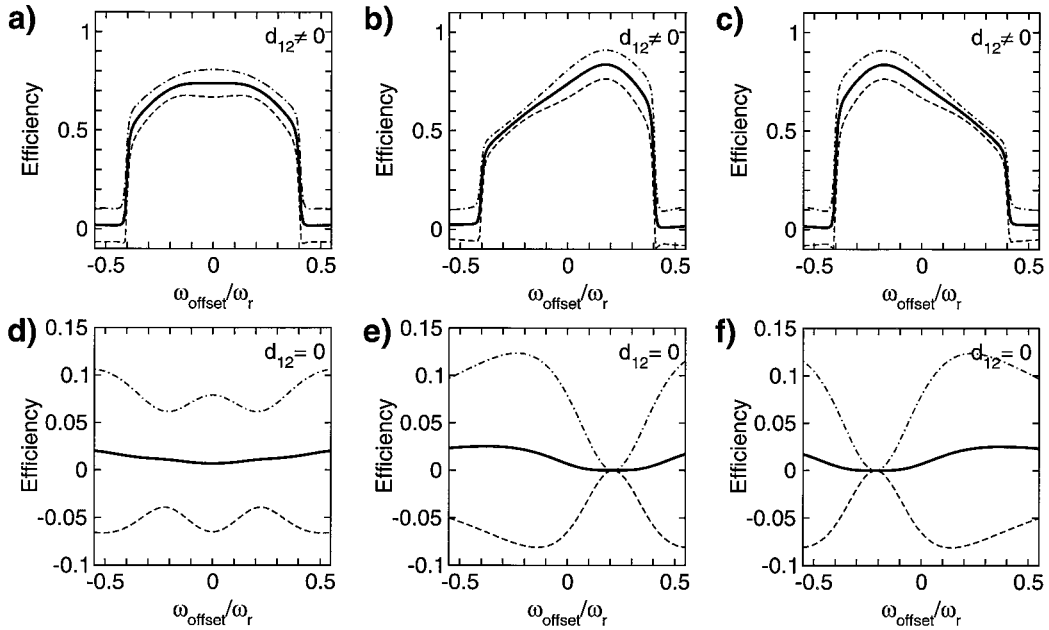

FIG. 8. Evaluation of Eqs. [44] and [45] for (a)–(c) a dipolar-coupled two-spin system with $d_{12} = 0.08 \cdot \omega_r$ and for (d)–(f) two isolated spins with $d_{12} = 0$ as a function of the frequency offset from the carrier of the RF field. The frequency offset zero is defined as the center between the chemical shifts of the two spins. An isotropic chemical-shift difference $\Omega_1^0 - \Omega_2^0 = 0.425\ \omega_r$, an average RF amplitude of $\bar{\omega}_1 = 0.445 \cdot \omega_r$, and an initial offset of $\Delta_{RF} = 0.18 \cdot \omega_r$ were used for the calculations. In all six plots the thick line shows the normalized intensity for the combination of four experiments according to the modulation scheme shown in Fig. 3c. The dashed lines and dash–dotted lines show the normalized intensities for the combination of scans 1 and 2 and scans 3 and 4, respectively. (a) and (d) show the total intensity summed over both spins. (b) and (e) show the signal intensity for spin 1 and (c) and (f) show the signal intensity for spin 2. The vastly improved suppression of the four-scan cycle for uncoupled spin intensity is clearly seen from (d) to (f).

dash–dotted lines show the results for a combination of the first and second, and the third and fourth, scans of Fig. 3c. It can clearly be seen that the suppression of the signal from uncoupled spins is significantly improved using the combination of all four amplitude modulation schemes.

3. EXPERIMENTAL

All experiments were done on a Varian-Chemagnetics CMX-400 Infinity spectrometer operating at a proton Larmor frequency of 400 MHz. The only exceptions are the data in Fig. 9 which were measured on a Varian-Chemagnetics CMX-300 Infinity spectrometer operating at a proton Larmor frequency of 300 MHz. Both instruments were equipped with a 2.5-mm double-resonance MAS probe. Unless indicated otherwise, the spinning frequency was set to 28 kHz in all experiments. Typical spinning-frequency stability varied depending on the sample but was always better than ±50 Hz. All experiments featured a variable-amplitude cross-polarization period with a tangential variation of the ^{13}C RF field (*26*). The adiabatic-passage Hartmann–Hahn (APHH) sweep was centered around the −1 Hartmann–Hahn matching condition with an initial offset of about 12 kHz for experiments at $\omega_r = 28$ kHz and correspondingly smaller at slower spinning frequencies. The sweep was approximated by 1000 discrete amplitude steps. A typical ^1H RF-field strength during CP was 100 kHz and the total mixing time was set to 1.5 ms. Continuous-wave decoupling of the protons was employed during the homonuclear ^{13}C recoupling using DREAM. The amplitude of this decoupling field was always equal to the amplitude of the TPPM decoupling (*46*) used during acquisition and was set sufficiently strong to avoid Hartmann–Hahn matching. Typically, the decoupling amplitude was around 140–160 kHz. The TPPM pulses were optimized for each experiment. Depending on the exact strength of the RF field, they had a duration of 3.2–3.6 μs and a phase offset ϕ of ±8 to ±10°.

The tangential RF variation of the DREAM sweeps was implemented by calculation of an array of 1000 discrete amplitudes for a full sweep. Different length sweeps were achieved by variation of the individual step sizes. The exact parameters for the different DREAM sweeps are indicated in the legends to the figures.

All experiments on sodium propionate were performed on a sample enriched to 99% $^{13}C_2$ on C-2 (methylene group) and C-3 (methyl group). The zinc acetate sample was crystallized from a solution of ca. 5% fully labeled 1,2-$^{13}C_2$-zinc acetate and ca. 95% natural-abundance zinc acetate in water. The sample of fully labeled [U-^{13}C] tyrosine was purchased from Cambridge Isotope Laboratories, Inc. (Andover, MA) and used without further purification.

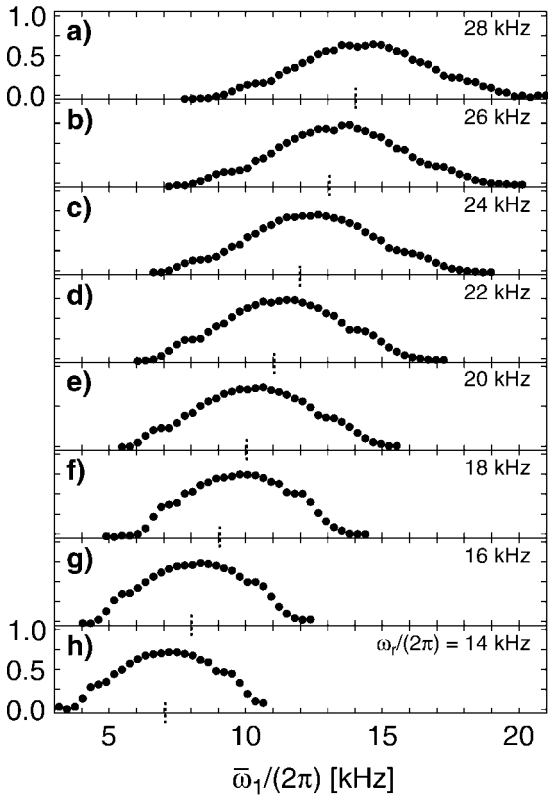

FIG. 9. Experimental signal intensity after DREAM filtering as a function of the average DREAM amplitude for a series of spinning frequencies ranging from (a) $\omega_r/(2\pi) = 28$ kHz to (h) $\omega_r/(2\pi) = 14$ kHz in steps of 2 kHz at a $B_0 = 7.0$ T static magnetic field. The pulse sequence of Fig. 3a was used. For each of the plots the vertical scale is normalized to the total intensity of a cross-polarization experiment at the corresponding spinning frequency. The total sweep time was set $\tau = 8$ ms. For (a) to (e) an initial amplitude offset $\Delta_{RF} = 5.2$ kHz and for (f) to (h) $\Delta_{RF} = 3.9$ kHz was used. A doubly labeled sample of sodium propionate was used. The dashed marks on the frequency axis mark the expected DREAM recoupling condition.

Simulations were programmed in C^{++} using the GAMMA spin-simulation environment (*47*). All simulations are powder averages of 300 orientations, where the individual orientations were determined by the method of Cheng and colleagues (*48*).

TABLE 2
Simulation Parameters for Sodium Propionate and Zinc Acetate

	2,3-$^{13}C_2$-Sodium propionate		1,2-$^{13}C_2$-Zinc acetate	
	CH_3	CH_2	CH_3	COO^-
δ	−670 Hz	−2400 Hz	−2310 Hz	−8040
η	1	0.64	0.5	0.32
(α, β, γ)	(0°, 0°, 0°)	(90°, 30°, 0°)	(0°, 0°, 0°)	(0°, 90°, 0°)
$\Delta\sigma_{iso}$	1858 Hz		16478 Hz	
d_{CC}	−2250 Hz[a]		−2324 Hz[b]	
J_{CC}	36 Hz		52 Hz	

Note. The Euler angles rotate from the PAS of the CSA to the PAS of the dipolar interaction.
[a] $|\overrightarrow{rCC}| = 1.5$ Å (estimated).
[b] $|\overrightarrow{rCC}| = 1.484$ Å.

The time dependence of the Hamiltonian was approximated by subdividing each rotor period into 500 time steps with a time-constant Hamiltonian. The parameters used for the simulations of zinc acetate and sodium propionate are summarized in Table 2.

4. RESULTS AND DISCUSSION

4.1. Spin-Pair Filters

In the following, the features of the DREAM recoupling scheme are characterized experimentally in the context of a two-spin filter but the basic properties (e.g., the transfer efficiency) are the same for the application as a mixing sequence in two-dimensional correlation experiments. The pulse scheme for the spin-pair filter is shown in Fig. 3b. The intensity of the resulting NMR signal as a function of the RF-field strength at the center of the sweep is shown in Fig. 9 for several different spinning frequencies. The carrier frequency was approximately (but not exactly to avoid interference by the J-coupling) centered between the two carbon resonances. The offset from the exact center between the two resonances was about 270 Hz, which is significantly more than the size of the J-coupling. A sample of 2,3-$^{13}C_2$-sodium propionate was used in these experiments. As expected, maximum intensity for the spin-pair filtered signal is found when the sweep is centered around the HORROR condition (Eq. [17]), marked by a thick dotted tick mark on the x-axis of Fig. 9. The efficiency of the recoupling process for a matched sweep is around 75% referenced to the signal intensity of a normal cross-polarization experiment at the same spinning frequency. The efficiency does not depend significantly on the MAS frequency in the range between 14 and 28 kHz. The independence from the spinning frequency is due to the rather small isotropic chemical-shift difference between the two resonances of the doubly labeled 2,3-$^{13}C_2$-sodium propionate.

The chemical-shift offset dependence of the DREAM sequence can be measured by changing the carrier frequency of the RF irradiation. The results of two such experiments, at the MAS frequencies of 28 and 14 kHz, are shown in Figs. 10a and 10b, respectively. The open markers show the results from exact numerical simulation using the GAMMA (*47*) simulation package to solve the Liouville–von Neumann equation. The parameters used for the simulation are summarized in Table 2. Considering that there are no adjustable parameters in this simulation, the agreement with the experiment is very good. The solid line shows the calculated filter efficiency based on Eq. [45]. The chemical-shift dependence is smaller at higher RF-field strength (Fig. 10a) and is more pronounced at slower MAS frequencies and correspondingly lower RF fields (Fig. 10b). The difference between the solid line on the one hand and the experimental data and numerical simulations on the other hand can be explained by nonadiabatic behavior of part of the dipolar-coupled pairs in the sample during the amplitude sweep. Although the

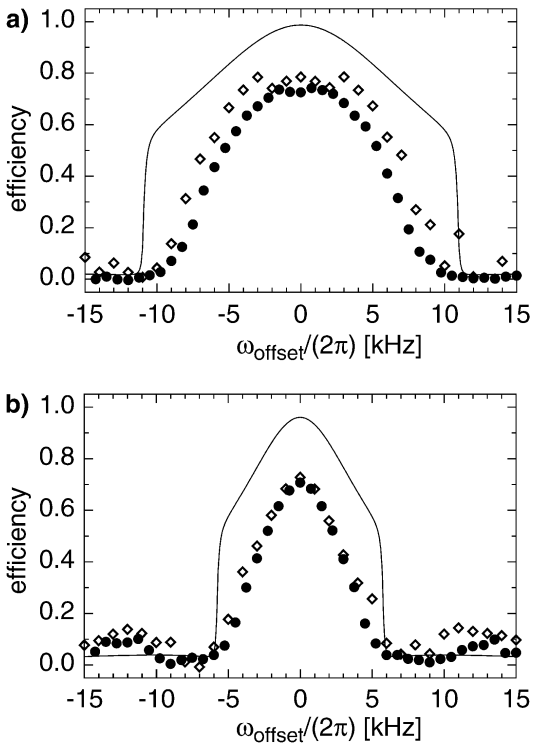

FIG. 10. Two-spin filter efficiency in doubly labeled 2,3-$^{13}C_2$-sodium propionate as a function of the carrier offset from the center between the two resonances at a spinning speed of (a) $\omega_r/(2\pi) = 28$ kHz and (b) $\omega_r/(2\pi) = 14$ kHz. The efficiency is defined as the experimental intensity normalized to the intensity obtained from a cross-polarization experiment at the same spinning frequency. The filled circles are the experimental data. The open diamonds correspond to numerical simulations with the parameters described in the text. The line corresponds to evaluation of Eqs. [44] and [45] with the parameters which are given below and in Table 2. In both (a) and (b) the total length of the tangential sweep was 8 ms. The center of the sweep was set to 13.9 and 7.8 kHz, corresponding to about $0.5 \cdot \omega_r/(2\pi)$ with an initial offset of 5.2 and 3.9 kHz for (a) and (b), respectively.

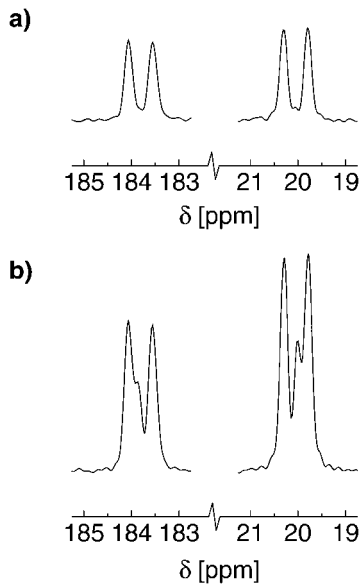

FIG. 11. (a) DREAM spin-pair filtered and (b) cross-polarization spectrum of a sample of 5% labeled 1,2-$^{13}C_2$-zinc acetate at a spinning speed of $\omega_r/(2\pi) =$ 28 kHz. For the amplitude variation of the DREAM experiment a total sweep length of 12 ms was used. The central amplitude of the sweep was set to 11.1 kHz with an initial offset of 2.8 kHz. The carrier frequency of the RF field was placed in the center between the two resonances.

size of effective dipolar coupling $d'_{k\ell}(T)$ is not very dependent on T, it strongly depends on the orientation of the crystallite as expressed by the angle $\theta_{k\ell}$ (See Appendix). This leads to a distribution of effective dipolar coupling constants. Spin systems with small couplings do not behave adiabatically under the experimental conditions chosen and give rise to the differences between the simplified model and the experimental and numeric data in Fig. 10.

Figure 11 shows ^{13}C spectra of 5% doubly labeled zinc acetate with (Fig. 11a) and without (Fig. 11b) spin-pair filtering. The fully labeled zinc acetate leads to a J-doublet for both lines. The natural-abundance zinc acetate leads to a singlet for each of the two resonances. The center of gravity of the doublet is shifted from the resonance position of the singlet due to second-order effects. This effect has been described before for slower spinning (*2*, *49*). This sample has a much larger chemical-shift difference and was used to investigate the dependence of the filter efficiency on the RF amplitude at the center of the sweep ($\bar{\omega}_1$) and on the carrier offset from the center between the two chemical shifts (ω_{offset}). The dependence of the DREAM filter efficiency on $\bar{\omega}_1$ for a fixed spinning frequency of 28 kHz is shown in Fig. 12. Taking into account the chemical-shift offsets of the two resonances in zinc acetate the HORROR condition is fulfilled for a spinning frequency of 28 kHz at an RF field of about 12 kHz. This RF-field strength is about 2 kHz lower than the expected resonance condition for a spin pair with a small chemical-shift difference. The decrease is caused by the

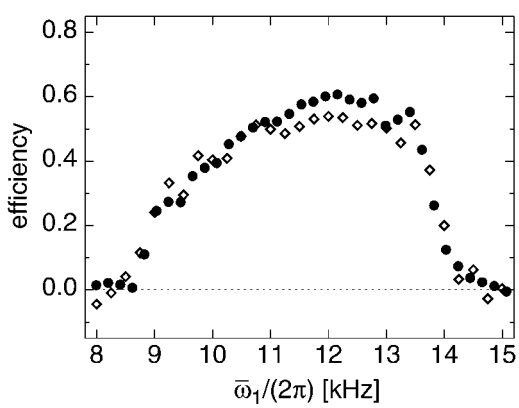

FIG. 12. Variation of the central amplitude $\bar{\omega}_1$ of the sweep. The same parameters were used as for the spectrum shown in Fig. 11a with the exception of the central amplitude. The filled circles are the experimental data and the open diamonds represent the simulated data.

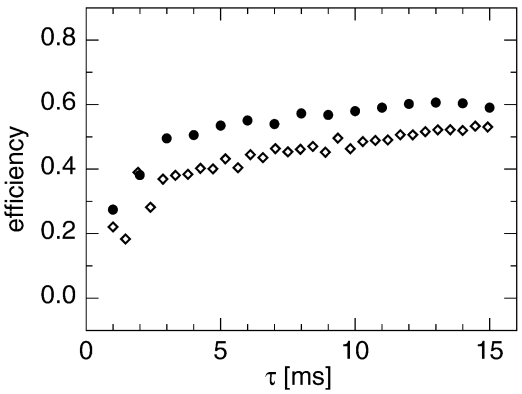

FIG. 13. Variation of the total length of the sweep. The filled circles are the experimental data. The same parameters were used as for the spectrum of Fig. 11a. For short durations of the sweep ($\tau < 1.5$ ms) incomplete suppression of single-quantum coherence signals made accurate determination of the double-quantum filter efficiency difficult. As a consequence the different signals were not deconvoluted, but simply the maximum intensity was taken. The open diamonds represent the simulated data.

large isotropic chemical shifts which contribute to the strength of the effective RF field. Since it is the sum of the effective RF-field strengths which are matched to the spinning frequency according to Eq. [17], the amplitude of the RF field at the HORROR condition becomes smaller. The open diamonds in Fig. 12 correspond to simulated data and follow closely the experimental behavior. The maximum efficiency of the two-spin filter is about 60% and somewhat lower than in sodium propionate. The reduction of the filter efficiency is a consequence of the larger isotropic chemical-shift difference of the two coupled spins. The efficiency is, however, expected to increase with higher spinning frequencies.

Figure 13 shows the dependence of the filter efficiency on the variation of the total sweep time τ. The maximum efficiency for zinc acetate is almost reached for a sweep time around 3–7 ms. The same behavior was previously observed in sodium propionate. The simulated data are again included as open diamonds and the agreement between simulated and experimental data is reasonable.

The offset dependence of the DREAM filter efficiency in zinc acetate is shown in Fig. 14. The filled dots in Fig. 14a are the experimental overall recoupling efficiency (sum magnetization) while the filled dots in Figs. 14b and 14c show the filter efficiency for the two resonances separately. Simulated data are again included as open markers. The simulated data in Figs. 14b and 14c were corrected for the experimentally determined unequal cross-polarization efficiencies of the CH_3 and CO resonances. The adiabatic sweep exchanges the intensities of both spins during the mixing time τ. The cross polarization to the CH_3-group is more efficient and, therefore, the normalized signal on the CO group is more intense.

The dependence of the DREAM filter efficiency as a function of the sweep width Δ_{RF} is shown in Fig. 15, where $\bar{\omega}_1$ was set to the HORROR condition. The DREAM filter efficiency is good as long as the initial offset is chosen to be larger than ca. 1.5 kHz. Such an offset ensures a reasonable initial tilt angle, $\Theta_{12}(0) \approx 15^\circ$ for the largest dipolar coupling. The total sweep time was kept constant at $\tau = 8$ ms. Therefore, the adiabaticity decreases with increasing Δ_{RF}, leading for $\Delta_{RF} > 2.5$ kHz to a decreased DREAM filter efficiency and an increase in the intensity of the unwanted signals from single spins which are marked by squares in Fig. 15.

4.2. Two-Dimensional Correlation Experiments

Figure 3a shows how the DREAM sequence can be incorporated into a two-dimensional correlation experiment. During the mixing time of the experiment, cw decoupling was applied on

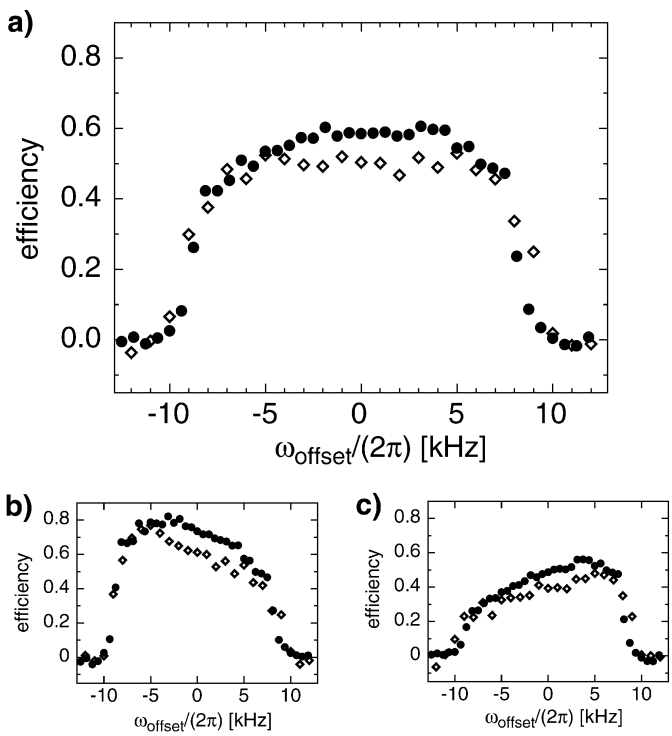

FIG. 14. Variation of the carrier frequency of the RF irradiation. The same parameters were used as for the spectrum of Fig. 11a. The frequency axis is referenced to the center between the two resonances. (a) The total experimental double-quantum efficiency calculated by the integration of all lines from 1,2-$^{13}C_2$-zinc acetate divided by the intensity of the same lines from a cross-polarization experiment. The experimental data are shown as filled circles. The open diamonds represent simulated data. (b) The normalized intensity of the carbonyl resonance normalized by the intensity of the methyl resonance from a cross-polarization experiment. Experimental data are marked by filled dots. The open diamonds represent simulated data for the carbonyl resonance of zinc acetate. (c) The normalized intensity of the methyl resonance normalized by the intensity of the carbonyl resonance from a cross-polarization experiment. The open diamonds represent simulated data. The strong difference in behavior between the two sets of data indicate both the uneven polarization by the cross polarization and the different projection onto the RF field as a function of the frequency offset.

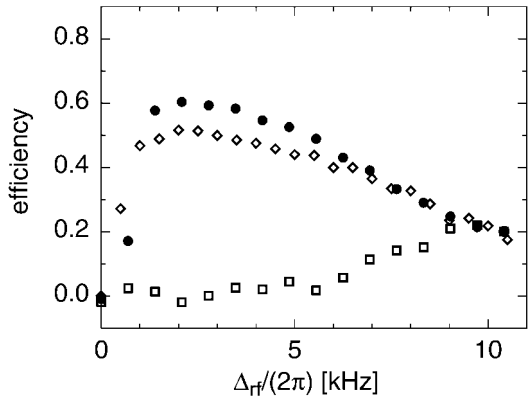

FIG. 15. Variation of the initial offset from the central amplitude of the sweep. The same parameters were used as for the spectrum of Fig. 11a with the exception of the initial offset. The filled circles show the normalized intensity of the signals from the 5% doubly labeled zinc acetate while the open squares show the intensity of the natural-abundance zinc acetate. The open diamonds represent simulated data for a dipolar-coupled spin pair with parameters as described in the text and Table 2.

the proton channel. During t_1 and t_2 TPPM decoupling was used. A 2D spectrum of sodium propionate with a DREAM sweep of $\tau = 8$ ms duration is shown in Fig. 16. This sweep has an adiabaticity parameter of $a(T) \geq 4.3$ for a crystallite with a "typical" dipolar interaction of 1.5 kHz. This value for the dipolar coupling is the weighted average over the powder distribution of the (absolute value of the) dipolar coupling in sodium propionate. Most of the intensity is observed in the cross peaks, indicating an efficient transfer of polarization as expected for an adiabatic sweep. This does not mean, however, that 100% of the polarization is transferred, because, according to Eq. [46], the intensity of the cross peaks is scaled by the projection onto the effective field. Because of the double-quantum mechanism, the cross peaks appear with negative intensity.

The $\pm\frac{\pi}{2}$ pulse in alternating scans after the DREAM sequence (see Fig. 3a) is necessary to suppress components of the density operator that are orthogonal to the RF field at the beginning of the DREAM sequence. The phase of this pulse is aligned with the phase of the DREAM sweep. The orthogonal components decay due to RF-field inhomogeneities for longer DREAM periods and tend to give rise to dispersive components in the lineshape. Figure 17 shows a two-dimensional ^{13}C–^{13}C correlation spectrum of sodium propionate with (Fig. 17a) and without (Fig. 17b) the $\pm\frac{\pi}{2}$ pulse for a short DREAM mixing time of 0.5 ms. The corresponding adiabaticity parameter is $a = 0.26$.

The cycling of the amplitude shapes (see Fig. 3c) was not used for the two-dimensional experiments. Therefore, coupled spins lead to negative cross peaks and no diagonal peaks and uncoupled spins to positive diagonal peaks. Application of the shape cycle and inversion of the receiver phase between alternating scans would lead, for the coupled spins, to negative cross peaks and to negative diagonal peaks. The intensities of the cross and diagonal peaks become equal for all angles $\vartheta \to \pi/2$. This can be seen by adding the columns in Table 1 and assuming equal initial intensity for each of the sites ($a_1 = a_2$). It would fully suppress uncoupled spins according to the same principle as the spin-pair filter (see Section 2.4). Such an experiment might be advantageous for selectively labeled samples with a high natural abundance background.

In this paper we concentrated on the characterization of the DREAM experiment in the simple case of two-spin systems. Nevertheless, we will now briefly discuss the application to larger spin systems. An experimental two-dimensional DREAM correlation spectrum of uniformly ^{13}C-labeled tyrosine is shown in Fig. 18 for a short mixing time of 0.5 ms. For larger spin systems, the observation of spectra at short mixing times leads to spectra that are easier to interpret (analogous, e.g., to the situation in chemical exchange or spin-diffusion spectra which are most informative in the initial-rate regime) than the spectra at longer mixing times. Although the adiabatic condition is violated, all nearest-neighbor correlations can be observed in the spectrum. The adiabaticity parameter is about 0.3 for two directly bonded carbon spins. In some cases, relayed transfer over two bonds can also be seen. These relayed correlations are indicated by arrows in Fig. 18 and can be recognized in the spectrum as positive cross peaks. The different signs of cross peaks with even or odd numbers of transfer steps can be considered one of the advantages of double-quantum coherence transfer. It can clearly be seen that the recoupling takes place over the entire chemical-shift range. Both the correlation between the carbonyl and the C^{α} and that between the C^{α} and the C^{β} carbons are present.

The multispin spectrum is not symmetric about the diagonal, which is clearly seen in Fig. 18. There are a number of sources for asymmetric cross-peak intensities. One source is the variation in cross-polarization efficiencies for the different resonances (*50*). In our case, however, the dominant reason is different. While all coupled spin pairs irrespective of the chemical-shift offsets go through the HORROR condition at some point during the DREAM sweep, they do not do so at the same time. Therefore, the amplitude of the cross peaks in many-spin systems depends on the order in which different transitions of a system with more than two spins pass through the HORROR condition. If the experiment of Fig. 18 is performed with a down–up ramp (Fig. 3c, third scan) instead of an up–down ramp (Fig. 3c, first scan) the resulting spectrum is the same as that of Fig. 18 but mirrored about the diagonal. Obviously, adding up the two different spectra leads to a symmetric spectrum. The details of the spin dynamics in fully labeled compounds is currently under investigation.

4.3. Practical Considerations

For the practical implementation of the DREAM recoupling sequence it is in general not necessary to take into account all parameters which influence the behavior of the system

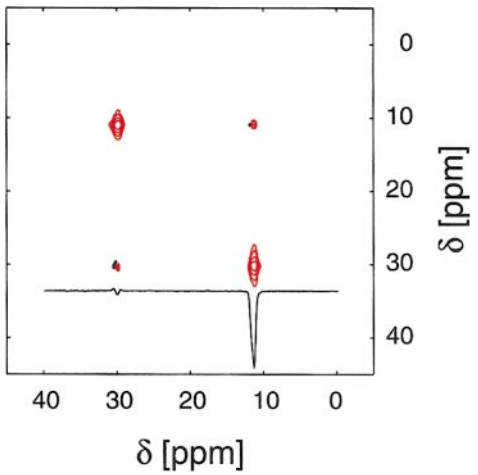

FIG. 16. Two-dimensional correlation spectrum of a sample of fully labeled 2,3-$^{13}C_2$-sodium propionate. The DREAM sweep of 8 ms was applied with the carrier frequency set to 100 ppm, with $\bar{\omega}_1 = 11.5$ kHz, and $\Delta_{RF} = 4$ kHz. Contours are placed at $-40, -20, -10, -5$, and -2.5% of the maximum absolute intensity in the data set.

during the DREAM experiment. To obtain good (although not optimized) results, it is sufficient to follow some simplified rules. The DREAM sequence has four parameters: the average RF-field amplitude, $\bar{\omega}_1$, the initial deviation of the RF field from its average value, Δ_{RF}, the total length of the DREAM period, τ, and the shape parameter, d_{est}. With these parameters, the amplitude sweep is completely defined according to Eq. [29].

The length τ must be longer than $1/d_{k\ell}$ and short compared to the relevant relaxation times $T_{1\rho}$ and T_{1d}^{DQ}. Here $d_{k\ell}$ denotes the dipolar-coupling constant that mediates the transfer and $T_{1\rho}$ and T_{1d}^{DQ} denote the rotating frame relaxation times for the spin-locked magnetization far from the HORROR condition and of a "HORROR-type" dipolar state at the HORROR condition. For a ^{13}C–^{13}C one-bond interaction, $\tau \geq 0.5$ ms leads already to strong cross peaks in a 2D spectrum, maximum transfer is reached after 3–7 ms. The value of d_{est} defines the shape for the amplitude sweep. Large values of d_{est} lead to almost linear amplitude sweeps, and small values to a pronounced tangential form. The optimum choice of d_{est} helps to minimize the sweep time τ. We distinguish three cases.

(i) If the width of the spectrum (or the part of it involved in polarization transfer) is much smaller than the MAS frequency (fast spinning limit), we set $\bar{\omega}_1 \approx 0.5 \cdot \omega_r$ and $\Delta_{RF} \approx 2 \cdot d_{k\ell}$, where $d_{k\ell}$ is an estimate for the largest dipolar coupling in the system. For directly bound carbons, $d_{k\ell}/(2\pi) \approx 2$ kHz and $\Delta_{RF}/(2\pi) \approx 4$ kHz. Furthermore $d_{est} \approx d_{k\ell}$ and, again for carbon, $d_{est}/(2\pi) \approx 2$ kHz. The length τ is chosen as indicated in the preceding paragraph.

(ii) If the width of the spectrum is not much smaller than the MAS frequency, but still smaller than about $\pm 0.25 \cdot \omega_r$, practical values for DREAM are $\bar{\omega}_1 \approx 0.45 \cdot \omega_r$ (somewhat smaller than above because the effective HORROR condition occurs at lower applied fields in the presence of chemical-shift offsets) and $\Delta_{RF} \approx 0.2 \cdot \omega_r$. A good compromise for the shape parameter is $d_{est} \approx 0.5 \cdot \Delta_{RF} \approx 0.1 \cdot \omega_r$. The length τ is chosen as indicated above.

(iii) If the width of the spectrum exceeds $\pm 0.25 \cdot \omega_r$, the DREAM recoupling will become frequency selective and spins outside the specified range will not significantly contribute to the spin dynamics. However, it is possible to recouple a *single* isolated spin pair (or a number of resonances grouped around two resonances) with an isotropic chemical-shift difference up to about $0.9 \cdot \omega_r$. In this case, there is a single DREAM condition with an amplitude $\bar{\omega}_1$ smaller than $\frac{1}{2}\omega_r$. The amplitude variation should be centered around this condition

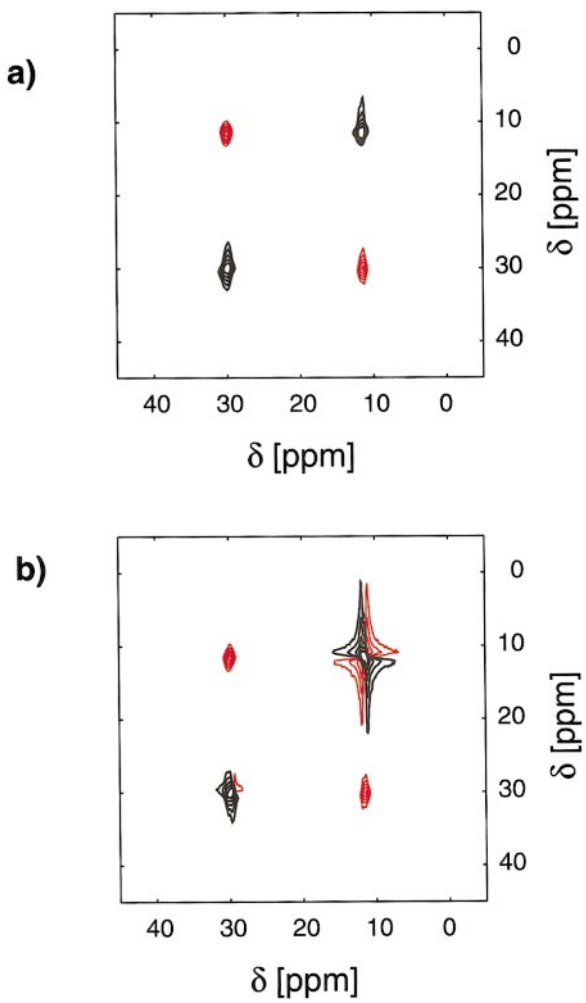

FIG. 17. Two-dimensional correlation spectrum of a sample of fully labeled 2,3-$^{13}C_2$-sodium propionate (a) with and (b) without the use of a purge pulse after the sweep. For both spectra the total length of the sweep was 0.5 ms. All other settings were as in Fig. 16. Contours are placed at $-40, -20, -10, -5, -2.5, 2.5, 5, 10, 20$, and 40% of the maximum positive intensity in the data set.

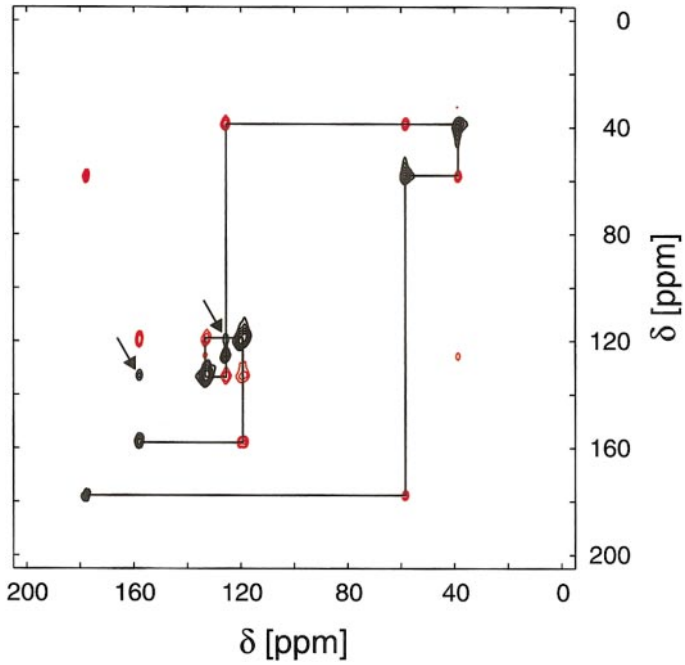

FIG. 18. Two-dimensional correlation spectrum of [U-^{13}C] tyrosine using the pulse sequence of Fig. 3. The total duration of the sweep was set to 0.5 ms, leading to a nonadiabatic behavior. The amplitude of the sweep at the center point was chosen to be $\bar{\omega}_1 = 11.5$ kHz with an initial offset of $\Delta_{RF} = 3.75$ kHz. The carrier frequency was set around 100 ppm. A total of 128 t_1 increments with four scans each were acquired. The lines indicated the directly bonded carbon atoms while the arrows indicated cross peaks in phase with the signals on the diagonal. A resolution of 39 and 195 Hz per point was set in t_2 and t_1, respectively. The $\pm\frac{\pi}{2}$ purge pulse had a duration of 2.6 μs. Contours were placed at -40, -20, -10, -5, -2.5, 2.5, 5, 10, 20, and 40% of the maximum positive intensity in the data set.

$\sqrt{(\Omega_1^0)^2 + (\bar{\omega}_1)^2} + \sqrt{(\Omega_2^0)^2 + (\bar{\omega}_1)^2} = \omega_r$ and $\Delta_{RF} \approx 2 \cdot d_{12}$ can be used.

5. CONCLUSIONS

The performance of the DREAM adiabatic dipolar-recoupling scheme was characterized in the context of one-dimensional and two-dimensional experiments. The experimental results are in qualitative agreement with predictions based on a simplified analytical model and in excellent quantitative agreement with exact spin-dynamic calculations.

The advantages of the adiabatic schemes, namely a broad matching behavior and a high transfer efficiency, have both been realized in the examples investigated. For spin pairs, an efficient exchange of populations is obtained by a DREAM sweep and all intensity is found in the cross peaks of the two-dimensional correlation spectrum. Some overall intensity loss is caused by projections onto the effective-field directions and deviations from adiabaticity. Therefore, the spin-pair filter efficiency is less than 100% but was found to be between 70 and 80% for sodium propionate and in excess of 60% for zinc acetate.

A four-shape cycle was introduced which leads to a better suppression of single-spin signals in spin-pair filtering experiments.

It was demonstrated that a two-dimensional DREAM correlation experiment of a uniformly labeled amino acid maps out the complete molecular connectivity. The DREAM sequence seems generally applicable to detect the connectivity in uniformly labeled samples. It provides a new tool for resonance assignments and, if long-range dipolar interactions can be detected, for structure determination. The experiment seems particularly attractive in connection with fast MAS, as the broadbandedness of the experiments increases with increasing MAS spinning frequency. However, applications where the DREAM sequence is used in a frequency-selective manner are also conceivable and have recently been reported (*51, 52*) using correspondingly slower MAS rates.

APPENDIX

The Fourier components of the spatial part of the chemical-shift interaction are given by

$$\Omega_k^{(\pm 1)} = \frac{\gamma B_0}{3\sqrt{2}}\delta_k \sin(\theta_k) e^{\pm i\varphi_k}[(3 - \eta_k \cos(2\chi_k))\cos(\theta_k) \pm i\eta_k \sin(2\chi_k)]$$

$$\Omega_k^{(\pm 2)} = \frac{\gamma B_0}{6}\delta_k e^{\pm 2i\varphi_k}\left[\frac{3}{2}\sin^2(\theta_k) + \frac{\eta_k}{2}(1 + \cos^2(\theta_k))\cos(2\chi_k) \mp i\eta_k \cos(\theta_k)\sin(\chi_k)\right]. \quad \text{[A-1]}$$

Here, δ_k and η_k denote the anisotropy and asymmetry of the CSA tensor and the three Euler angles $\varphi_k, \theta_k, \chi_k$ describe the time-independent transformation from the rotor-fixed coordinate system to the principal-axis system of the CSA tensor of spin k.

The Fourier components of the spatial part of the dipolar interaction are given by

$$d_{k\ell}^{(\pm 1)} = -\frac{d_{k\ell}}{2\sqrt{2}}\sin(2\theta_{k\ell})e^{\pm i\varphi_{k\ell}}$$

$$d_{k\ell}^{(\pm 2)} = \frac{d_{k\ell}}{4}\sin^2(\theta_{k\ell})e^{\pm 2i\varphi_{k\ell}} \quad \text{[A-2]}$$

$$d_{k\ell} = -\frac{\mu_0 \gamma^2 \hbar}{4\pi r_{k\ell}^3}.$$

The Euler angles $\varphi_{k\ell}, \theta_{k\ell}$ describe the transformation from the rotor-fixed coordinate system of the dipolar-coupling tensor between spins k and ℓ to the principle-axis system.

The scaling coefficients for the dipolar part of the Hamiltonian in the tilted frame of reference are given by

$$\begin{aligned} A^{\mathrm{d}}_{k\ell}(T) &= 2\cos\vartheta_k\cos\vartheta_\ell - \sin\vartheta_k\sin\vartheta_\ell \\ B^{\mathrm{d}}_{k\ell}(T) &= -\frac{1}{2} - \frac{1}{2}\cos\vartheta_k\cos\vartheta_\ell + \sin\vartheta_k\sin\vartheta_\ell \\ R^{\mathrm{d}}_{k\ell}(T) &= -\cos\vartheta_k\sin\vartheta_\ell - \frac{1}{2}\sin\vartheta_k\cos\vartheta_\ell \quad . \\ V^{\mathrm{d}}_{k\ell}(T) &= -\sin\vartheta_k\cos\vartheta_\ell - \frac{1}{2}\cos\vartheta_k\sin\vartheta_\ell \\ Q^{\mathrm{d}}_{k\ell}(T) &= \frac{1}{2} - \frac{1}{2}\cos\vartheta_k\cos\vartheta_\ell + \sin\vartheta_k\sin\vartheta_\ell \end{aligned} \qquad \text{[A-3]}$$

and the scaling factors for the J-coupling part of the Hamiltonian are given by

$$\begin{aligned} A^{J}_{k\ell}(T) &= \cos\vartheta_k\cos\vartheta_\ell + \sin\vartheta_k\sin\vartheta_\ell \\ B^{J}_{k\ell}(T) &= 1 + \cos\vartheta_k\cos\vartheta_\ell + \sin\vartheta_k\sin\vartheta_\ell \\ R^{J}_{k\ell}(T) &= \sin\vartheta_k\cos\vartheta_\ell - \cos\vartheta_k\sin\vartheta_\ell \\ V^{J}_{k\ell}(T) &= -\sin\vartheta_k\cos\vartheta_\ell + \cos\vartheta_k\sin\vartheta_\ell \\ Q^{J}_{k\ell}(T) &= -1 + \cos\vartheta_k\cos\vartheta_\ell + \sin\vartheta_k\sin\vartheta_\ell \end{aligned} \qquad \text{[A-4]}$$

In Equations [A-3] and [A-4] the angles ϑ_k and ϑ_ℓ are the tilt angles between the direction of the z-axis in the rotating frame and the direction of the z-axis in the tilted frame, which is aligned with the direction of the effective field of spins k and ℓ, respectively. All angles are T-time dependent.

ACKNOWLEDGMENTS

Scientific discussions with Aswin Verhoeven, Jacco van Beek, Melanie Nijman, Dr. Phil Williamson, Dr. Pierre Robyr, and Dr. Macro Tomaselli are gratefully acknowledged. Scientific advice by and scientific discussions with Dr. Andreas Detken were instrumental in the final stages of this work. Jan van Os (Nijmegen) provided excellent technical support. Financial support by the Dutch and the Swiss National Science foundations is acknowledged.

REFERENCES

1. B. H. Meier and W. L. Earl, *J. Chem. Phys.* **85,** 4905 (1986).
2. B. H. Meier and W. L. Earl, *J. Am. Chem. Soc.* **109,** 7937 (1987).
3. M. H. Levitt, D. P. Raleigh, F. Creuzet, and R. G. Griffin, *J. Chem. Phys.* **92,** 6347 (1990).
4. R. Tycko and S. O. Smith, *J. Chem. Phys.* **98,** 932 (1993).
5. A. E. Bennett, J. H. Ok, R. G. Griffin, and S. Vega, *J. Chem. Phys.* **96,** 8624 (1992).
6. T. Gullion and S. Vega, *Chem. Phys. Lett.* **194,** 423 (1992).
7. T. Fujiwara, A. Ramamoorthy, K. Nagayama, K. Hioka, and T. Fujito, *Chem. Phys. Lett.* **212,** 81 (1993).
8. M. Baldus, M. Tomaselli, B. H. Meier, and R. R. Ernst, *Chem. Phys. Lett.* **230,** 329 (1994).
9. N. C. Nielsen, H. Bildsoe, H. J. Jakobsen, and M. H. Levitt, *J. Chem. Phys.* **101,** 1805 (1994).
10. Y. K. Lee, N. D. Kurur, M. Helmle, O. G. Johannessen, N. C. Nielsen, and M. H. Levitt, *Chem. Phys. Lett.* **242,** 304 (1995).
11. K. Takegoshi, K. Nomura, and T. Terao, *J. Magn. Reson.* **127,** 206 (1997).
12. D. M. Gregory, D. J. Mitchell, J. A. Stringer, S. Kiihne, J. C. Shiels, J. Callahan, M. A. Mehta, and G. P. Drobny, *Chem. Phys. Lett.* **246,** 654 (1995).
13. B. Q. Sun, P. R. Costa, D. Kocisko, P. T. J. Lansburgy, and R. G. Griffin, *J. Chem. Phys.* **102,** 702 (1995).
14. M. Hohwy, H. J. Jakobsen, M. Eden, M. H. Levitt, and N. C. Nielsen, *J. Chem. Phys.* **108,** 2686 (1998).
15. C. M. Rienstra, M. E. Hatcher, L. J. Mueller, B. Q. Sun, S. W. Fesik, and R. G. Griffin, *J. Am. Chem. Soc.* **120,** 10602 (1998).
16. M. Hohwy, C. M. Rienstra, C. P. Jaroniec, and R. G. Griffin, *J. Chem. Phys.* **110,** 7983 (1999).
17. A. Brinkmann, M. Eden, and M. H. Levitt, *J. Chem. Phys.* **112,** 8539 (2000)
18. R. Verel, M. Baldus, M. Ernst, and B. H. Meier, *Chem. Phys. Lett.* **287,** 421 (1998).
19. R. Verel, M. Baldus, M. Nijman, J. W. M. van Os, and B. H. Meier, *Chem. Phys. Lett.* **280,** 31 (1997).
20. K. Takegoshi, K. Nomura, and T. Terao, *Chem. Phys. Lett.* **232,** 424 (1995).
21. P. R. Costa, B. Q. Sun, and R. G. Griffin, *J. Am. Chem. Soc.* **119,** 10821 (1997).
22. K. Nomura, K. Takegoshi, T. Terao, K. Uchida, and M. Kainosho, *J. Biomol. NMR* **17,** 111 (2000).
23. M. Baldus, D. G. Geurts, S. Hediger, and B. H. Meier, *J. Magn. Reson. A* **118,** 140 (1996).
24. S. Hediger, B. H. Meier, N. D. Kurur, G. Bodenhausen, and R. R. Ernst, *Chem. Phys. Lett.* **223,** 283 (1994).
25. S. Zhang, C. L. Czekay, and W. T. Ford, *J. Magn. Reson. A* **111,** 87 (1994).
26. S. Hediger, B. H. Meier, and R. R. Ernst, *J. Chem. Phys.* **102,** 4000 (1995).
27. J. H. Shirley, *Phys. Rev.* **138B,** 979 (1965).
28. Y. Zur, M. H. Levitt, and S. Vega, *J. Chem. Phys.* **78,** 5293 (1983).
29. S. Vega, E. T. Olejniczak, and R. G. Griffin, *J. Chem. Phys.* **80,** 4832 (1984).
30. A. E. Bennett, R. G. Griffin, and S. Vega. Recoupling of homo- and heteronuclear dipolar interactions in rotating solids, *in* "NMR Basic Principles and Progress, Vol. 33 of NMR Basic Principles and Progress, Solid-State NMR IV," pp. 1–77. Springer-Verlag, Berlin, 1994.
31. B. H. Meier. Polarization transfer and spin diffusion in solid-state NMR, *in* "Advances in Magnetic and Optical Resonance" (W. S. Warren, ed.), Vol. 18, pp. 1–116. Academic Press, New York, 1994.
32. T. O. Levante, M. Baldus, B. H. Meier, and R. R. Ernst, *Mol. Phys.* **86,** 1195 (1995).
33. R. Tycko and G. Dabbagh, *Chem. Phys. Lett.* **173,** 461 (1990).
34. N. C. Nielsen, F. Creuzet, R. G. Griffin, and M. H. Levitt, *J. Chem. Phys.* **96,** 5668 (1992).
35. X. Feng, P. J. E. Verdegem, Y. K. Lee, D. Sandstrom, M. Eden, P. Boveegeurts, W. J. de Grip, J. Lugtenburg, H. J. M. de Groot, and M. H. Levitt, *J. Am. Chem. Soc.* **119,** 6853 (1997).
36. S. Hediger, B. H. Meier, and R. R. Ernst, *Chem. Phys. Lett.* **240,** 449 (1995).
37. C. Cohen-Tannoudji, B. Diu, and F. Laloe, "Quantum Mechanics," Wiley, New York, 1977.
38. M. Bak and N. C. Nielsen, *J. Chem. Phys.* **106,** 7587 (1997).
39. S. Hediger, B. H. Meier, and R. R. Ernst, *Chem. Phys. Lett.* **213,** 627 (1993).
40. S. Hediger, P. Signer, M. Tomaselli, R. R. Ernst, and B. H. Meier, *J. Magn. Reson.* **125,** 291 (1997).
41. M. Nijman, M. Ernst, A. P. M. Kentgens, and B. H. Meier, *Mol. Phys.* **98,** 161 (2000).
42. A. Wokaun and R. R. Ernst, *J. Chem. Phys.* **67,** 1752 (1977).

43. S. Vega, *J. Chem. Phys.* **68,** 5518 (1978).
44. J. Baum, M. Munowitz, A. N. Garroway, and A. Pines, *J. Chem. Phys.* **83,** 2015 (1985).
45. C. J. Hardy, W. A. Edelstein, and D. Vatis, *J. Magn. Reson.* **66,** 470 (1986).
46. A. E. Bennett, C. M. Rienstra, M. Auger, K. V. Lakshmi, and R. G. Griffin, *J. Chem. Phys.* **103,** 6951 (1995).
47. S. Smith, T. Levante, B. H. Meier, and R. R. Ernst, *J. Magn. Reson. A* **106,** 75 (1994).
48. H. H. Suzukawa, V. B. Cheng, and M. Wolfsberg, *J. Chem. Phys.* **59,** 3992 (1973).
49. T. Nakai and C. A. McDowell, *Mol. Phys.* **77,** 569 (1992).
50. S. Caldarelli and L. Emsley, *J. Magn. Reson.* **130,** 233 (1998).
51. J. Pauli, M. Baldus, B. van Rossum, H. J. M. de Groot, and H. Oschkinat, *BioChemBio* **2,** 272 (2001).
52. A. Detken, E. Hardy, M. Ernst, and B. H. Meier, *J. Biomol. NMR*, in press (2001).